Article published in

Additive Manufacturing, Vol. 57 (2022) 102982

https://doi.org/10.1016/j.addma.2022.102982

Topology optimization for 3D concrete printing with various manufacturing constraints

Minghao Bi [1], Phuong Tran [1], Lingwei Xia [2], Guowei Ma [2], and Yi Min Xie [1,*]

[1] Centre for Innovative Structures and Materials, School of Engineering, RMIT University, Melbourne, Victoria 3001, Australia

[2] Tianjin Key Laboratory of Prefabricated Building and Intelligent Construction, School of Civil and Transportation Engineering, Hebei University of Technology, Tianjin 300401, China

[*] Corresponding author.
E-mail address: mike.xie@rmit.edu.au (Y.M. Xie).

Abstract

The integration between 3D concrete printing (3DCP) and topology optimization (TO) enables the fabrication of structurally efficient components without expensive formwork and intensive labor. However, manufacturing constraints of 3DCP are impeding the integration between the two fields, and there has been limited research on this topic. In this paper, we address various manufacturing constraints of 3DCP within the bi-directional evolutionary structural optimization (BESO) framework. Firstly, a layer-wise sensitivity scheme is proposed to generate self-supporting designs in the user-defined print direction. Secondly, a novel continuous extrusion constraint is implemented to facilitate the continuous printing operation of the design. Thirdly, the anisotropy of the 3DCP process is simulated during optimization by employing a transverse isotropic material model. Fourthly, domain segmentation is introduced to facilitate modular construction, and each partitioned segment can be assigned with its favorable print direction. Finally, the algorithm's feasibility is demonstrated by constructing a topology optimized chair.

Keywords: Topology optimization, 3D concrete printing, Self-support, Manufacturing constraints, Large-scale additive manufacturing.

1. Introduction

Additive manufacturing (AM), also commonly known as 3D printing, allows the manufacture of complicated designs in a layer-by-layer process. Compared with its casting-based counterpart, AM's unique mechanism enables greater design flexibility in geometry and precision control in production [1]. With burgeoning interests and continuous refinement, AM has been successfully implemented in various industrial applications, such as aerospace [2,3], biomedicine [4], automotive [5], and architecture [6]. Research has recently been drawn to applying AM on a construction scale, facilitating automation and free-form designs in the architecture, engineering, and construction (AEC) industry. Among different strategies, 3D concrete printing (3DCP), which constructs large-scale structures by extruding cement-based material, is developing rapidly. Some recent examples of 3DCP in the construction industry include 3D concrete printed green walls [7], bespoke columns [8], and truss-shaped pillars [9].

Topology optimization (TO) is a field of study that seeks the optimum structural layout under the prescribed design conditions. By taking an iterative procedure, structurally inefficient areas are progressively removed until the design is refined to a desirable state. Introduced in the 1980s [10], TO has witnessed continuous development and extended into different methods, including homogenization method [10,11], solid isotropic material with penalization (SIMP) method [12–14], level set method [15–18], evolutionary structural optimization (ESO) method [19], bi-directional ESO (BESO) method [20,21], moving morphable component (MMC) method [22], and moving morphable void (MMV) method [23]. Interested readers should refer to the following reviews [24,25] for a comprehensive summary of different TO methods. The design freedom enabled by AM is well compatible with the concept of TO, whose geometrical complexity generally limits its application using traditional manufacturing methods. Extensive studies have been conducted in the literature to facilitate the integration between the two fields

[26–29]. For large-scale construction, the integration between 3DCP and TO opens up opportunities for fabricating spatially intriguing and structurally efficient structures.

Although the integration between 3DCP and TO shows great potential, there are still many challenges to be addressed first. Examples of such hurdles include the overhang angle to remain self-supporting [30], anisotropic behavior [31,32], compatible reinforcement strategy [33,34], continuous section and toolpath for better print quality [35,36], modular design strategy [37,38], and material shrinkage [39]. The overhang angle measures the inclination of downward-facing surfaces to the horizontal plane. Due to the gravitational force, cantilevering features may lose their self-supporting capacity if they exceed the maximum overhang angle limit, typically ranging from 70° to 90° depending on applications. Because of the nature of 3DCP, printed outcomes exhibit anisotropic structural behavior [31,32] and are subject to cracks on the surface due to shrinkage [39], which should be carefully considered during the design phase. Research has been conducted on incorporating reinforcements in tensile zones; different strategies include bar penetration [33], mesh reinforcement [40], fiber and micro-cable reinforcement [31,34]. For printers whose material feeding system is separated from the nozzle movement system, simultaneous stop-and-start operation for both systems can be challenging. In the meantime, 3DCP calls for continuous printing within the window of the setting time to avoid nozzle blockage due to material solidification [41]. In this regard, each printing layer and associated toolpath should be continuous to maximize print quality and efficiency. To bypass the strict overhang limit of 3DCP, some structural designs are partitioned into segments, which are printed separately and assembled together [37,38]. The manufacturing constraints mentioned above are commonly addressed during the post-processing stage, requiring extra design effort and potentially significant modifications. Consequently, the topology optimized design has to sacrifice its structural efficiency. In the worst scenario, the design may not be

manufacturable at all. In this regard, an explicit TO framework that incorporates various manufacturing constraints of 3DCP is needed to facilitate the integration between the two fields.

In this work, an integrated topology optimization framework is proposed to address various manufacturing constraints of 3DCP. In order to generate a self-supporting design, a layer-wise sensitivity scheme is introduced to mimic the layer-by-layer printing process. Different printing directions can be specified, and the generated design remains vertically aligned and continuous in each iteration. A novel continuous extrusion constraint is implemented to ensure the geometrical continuity of each layer, which enables uninterrupted nozzle movement during the fabrication process. Analogous to the concept of modular construction, domain segmentation is proposed to allow different print directions in each segment. The anisotropic behavior of 3DCP is also simulated in the framework by assuming a transverse isotropic material model in the finite element analysis (FEA). All manufacturing constraints above are compatible with each other. The BESO procedure is used in this paper for its compatibility with image-processing strategies using binary variables and good computational efficiency. In the experiment section, the algorithm's feasibility is tested by fabricating a topology optimized chair using 3DCP.

The main contributions of this paper are summarized as follows:

- A novel TO framework is proposed by considering various manufacturing constraints of 3DCP.
- The optimized design achieves self-supporting by ensuring vertical alignment in geometry.
- An innovative continuous extrusion constraint is presented to enable continuous movement and extrusion of the nozzle in 3DCP.

- The design domain of TO can be divided into sub-domains to allow favorable print direction in each segment and facilitate modular construction.
- Anisotropic behavior of 3DCP can be simulated in TO by assuming a transverse isotropic material model.
- Implementation of the algorithm is demonstrated by fabricating a topology optimized chair using 3DCP.

The remainder of the paper is organized as follows: Section 2 reviews some related work in the literature about 3DCP and TO. Section 3 provides a detailed description of the proposed topology optimization framework. Numerical studies and experimental validation are presented in Sections 4 and 5, followed by concluding remarks in Section 6.

2. Related work

This section reviews existing 3DCP and TO studies in the literature related to our work. Current challenges and limitations are discussed, and the need for integration and improvements is highlighted.

2.1. Challenges of 3DCP

Numerous studies have investigated the influence of material mixture on the printability and mechanical properties of 3DCP [42–47]. In particular, the rheology of the mixture, governed by the initial yield stress and plastic viscosity, is a critical factor affecting the printability and buildability of the material [46]. Early material solidification leads to high pumping pressures within the nozzle, potentially blocking the pumping system and sabotaging the printing process. Contrarily, a mixture with high flowability may lose the capability to retain its shape and result in poor mechanical performance [41]. In principle, a desirable material should remain flowable within the pumping system and quickly solidify to carry its

own weight after deposition. Geometrically speaking, cantilevering features should be carefully designed to avoid the buckling of superimposed layers [46]. In practice, applications of 3DCP favor vertically aligned geometry with repetitive patterns [38,48–51] to minimize the risk of collapsing due to self-weight. Toolpaths are also designed to be continuous to maximize print quality and efficiency [38,48–51]. Due to the nature of layer-wise fabrication, the anisotropy is observed in 3DCP and is extensively studied in the literature [31,32,52]. The interface between vertical layers is subject to pores and defects, making the bonding between vertical layers weaker than horizontal layers under bending. The anisotropy of 3DCP should be carefully considered during the simulation and optimization process. Segmentation is a universally acknowledged strategy for large-scale structures with complex geometry to bypass the overhang limit of 3DCP [37,38,50]. The designs are partitioned into segments and printed separately in their favorable orientation, followed by assembly using grouting or chemical bonding. However, segmentation in the literature is carried out after the optimization process; an interactive and user-defined segmentation strategy within the topology optimization framework is desirable. For more details on 3DCP, interested readers are referred to the following reviews [35,41,53].

2.2. Topology optimization for concrete-based structures

The possibility of constructing topology optimized structures using cement-based materials has been explored in the literature. Jipa et al. [54] designed a topology optimized concrete slab based on the SIMP method. The fabrication of the slab began with binder jetting a stay-in-place sand formwork followed by casting ultra-high-performance fiber-reinforced concrete (UHPFRC) inside the formwork. In a subsequent study, Jipa et al. [55] presented a topology optimized stair prototype using FDM printed formwork and demonstrated how steel-fiber reinforcements could be used in combination with post-tensioning to enhance its structural performance. Søndergaard et al. [56] constructed a topology optimized component by casting

ultra-high-performance concrete (UHPC) using robotic abrasive wire-cutting of expanded polystyrene formwork. The production of the bespoke concrete prototype is realized through the prefabrication of six separate components to be joined on site. The Eggshell fabrication process developed by Burger et al. [57] combined large-scale FDM printing of formwork with the simultaneous casting of fast-hardening concrete, which was reported to be applicable to topology optimized concrete structures. A multi-physics topology optimization framework for 3D printed concrete structures was proposed by Vantyghem et al. [58], and a small-scale physical specimen was cast in concrete and loaded in a 3-point-bending test. The above work relied on 3D-printed formwork to support concrete casting, which requires a post-processing phase. Without needing formwork, Vantyghem et al. [37] constructed a post-tensioned concrete girder designed by topology optimization. Inspired by the 2D topology optimized result [59], the 3D concrete girder was subdivided into hollow parts printed separately and assembled later. During the assembly process, rebars and post-tensioning tendons were placed within the hollow parts, followed by subsequent grouting and post-tensioning. Martens et al. [60] developed a topology optimization framework for 3DCP considering the overhang constraint, self-supporting concrete slab design was generated, but no physical demonstration of the results was reported. Most topology optimized concrete structures in the literature depend on formwork, which may require additional design effort and labor for post-processing. Realization of topology optimized designs through 3DCP is currently limited, and a topology optimization framework addressing various manufacturing constraints of 3DCP is needed.

2.3. Topology optimization with different manufacturing constraints

Many studies have integrated an overhang angle constraint into the topology optimization framework. Gaynor and Guest [61] used a wedge-shaped filter to simulate the support condition at different overhang angles. A projection-based approach was proposed by Qian [62], where overhanging features are controlled using the projected overhang length. A layer-

wise strategy has been adopted by Langelaar in 2D [63] and 3D [64] to generate self-supporting designs at a 45° overhang angle. Allaire et al. [65] considered the overhang angle constraint in a level-set topology optimization framework. Zhang et al. [66] explored how the overhang angle and minimum size constraints can be considered simultaneously. Han et al. [67] considered both the overhang and the subtractive manufacturing constraint for a hybrid additive-subtractive manufacturing system. The method developed by Bi et al. [27] can generate self-supporting 3D designs at an arbitrary overhang angle. Van de Ven et al. [68] demonstrated how the front propagation method can be used to generate 3D self-supporting designs. Liu et al. [69] combined overhang angle and minimum length scale constraints to generate self-supporting infill structures. Compared with common additive manufacturing methods, the overhang constraint for 3DCP is much stricter (70–90°). It is worth noting that a 90° overhang constraint is identical to a casting constraint, whose integration within the topology optimization framework has been widely studied [70–72].

Material anisotropy can directly affect the structural performance of additively manufactured components. The study carried out by Chiu et al. [73] suggested that material anisotropy can significantly influence the optimization outcome. Mirzendehdel et al. [74] proposed a method to optimize anisotropic parts based on Tsai-Wu failure criteria.

Consideration of deposition path within topology optimization has been considered in previous studies. Liu and To [75] developed a topology optimization framework where deposition path planning is conducted in each layer using contour and skeleton paths. Papapetrou et al. [76] proposed a stiffness-based optimization method that maximizes path continuity by considering fiber orientation and infill pattern. However, global continuity of the geometry was not achieved in those previous studies.

Overall, work in the literature focuses on a general 3D printing setting rather than 3DCP. An integrated topology optimization framework that addresses multiple constraints of 3DCP demands research attention.

3. Methodology

This section systematically explains how different manufacturing constraints of 3DCP are integrated within the BESO topology optimization framework. The programming and computation of the proposed method are implemented in the Python platform.

3.1. BESO framework

In topology optimization, minimization of compliance, or equivalently maximization of stiffness, is an extensively studied area. Within the BESO topology optimization framework, the proposed topology optimization problem can be formulated as:

$$\begin{gathered} Minimize:\ C = \frac{1}{2}\boldsymbol{F^T U} \\ Subject\ to:\ \boldsymbol{KU} = \boldsymbol{F} \\ V^* - \sum_{i=1}^{n_x}\sum_{j=1}^{n_y}\sum_{k=1}^{n_z} V_{i,j,k}\rho_{i,j,k} = 0 \\ \rho_{i,j,k} = 1 \text{ or } \rho_{min} \\ \rho_{i,j,k} \geq \rho_{i,j,k+1} \\ \sum_{k=1}^{n_z} g_k = n_z,\ \ g_k \geq 1 \end{gathered} \tag{1}$$

where C, $\boldsymbol{K}$, $\boldsymbol{U}$, and $\boldsymbol{F}$ denote the mean compliance, the global stiffness matrix, the global displacement and force vectors, n_x, n_y, n_z are the number of elements in the principal axes, V^*, $V_{i,j,k}$ and $\rho_{i,j,k}$ represent the prescribed target volume, the individual element volume, and the design variable, respectively, g_k measures the number of enclosed regions in the k-th layer.

The self-support constraint $\rho_{i,j,k} \geq \rho_{i,j,k+1}$ ensures that solid elements are vertically supported by the elements below. The continuous extrusion constraint $\sum_{k=1}^{n_z} g_k = n_z$ requires each layer to have one single enclosed region.

In BESO, the Young's modulus of an element is interpolated as a function of the binary design variable:

$$E(\rho_{i,j,k}) = E_1 \rho_{i,j,k}^p \tag{2}$$

where E_1 denotes the Young's modulus of solid material, and p is the penalty exponent. The element stiffness matrix can then be interpolated as:

$$\boldsymbol{k_{i,j,k}} = \rho_{i,j,k}^p \boldsymbol{K_{i,j,k}^0} \tag{3}$$

After assembly, the global stiffness matrix can be formulated as:

$$\boldsymbol{K} = \sum_{n=1} \rho_{i,j,k}^p \boldsymbol{K_{i,j,k}^0} \tag{4}$$

where $\boldsymbol{K_{i,j,k}^0}$ represents the element stiffness matrix of the solid element. In this paper, a widely adopted value of 0.001 and three are specified for ρ_{min} and p, respectively.

The sensitivity of the objective function with respect to the design variable is derived as:

$$\alpha_{i,j,k} = \begin{cases} \dfrac{1}{2} \boldsymbol{u_{i,j,k}^T K_{i,j,k}^0 u_{i,j,k}} & when \;\; \rho_{i,j,k} = 1 \\ \dfrac{\rho_{min}^{p-1}}{2} \boldsymbol{u_{i,j,k}^T K_{i,j,k}^0 u_{i,j,k}} & when \;\; \rho_{i,j,k} = \rho_{min} \end{cases} \tag{5}$$

where $\boldsymbol{u_{i,j,k}}$ denote an element's nodal displacement vector.

To circumvent mesh-dependency and checkerboard problems, a filtering scheme is adopted to average the sensitivity numbers within a prescribed filter radius r_{min} as follows:

$$\alpha_{i,j,k}^{new} = \frac{\sum_{n=1}^{N} w(r_{ni})\,\alpha_n}{\sum_{n=1}^{N} w(r_{ni})}$$
$$w(r_{ni}) = r_{min} - r_{ni} \quad (n = 1, 2, \cdots, N) \tag{6}$$

where the filtered sensitivity number $\alpha_{i,j,k}^{new}$ is determined by weighting the original sensitivity number α_n within the filtering region based on a linear weight factor $w(r_{ni})$. N and r_{ni} denote the total number of elements within the filter and the distance between the filter center and element center.

To stabilize the optimization process, the sensitivity number in each iteration is averaged with its historical information:

$$\alpha_{i,j,k} = \frac{\alpha_{i,j,k}^{m} + \alpha_{i,j,k}^{m-1}}{2} \tag{7}$$

where m is the current iteration number. The history averaging scheme prevents oscillations in the evolutionary history and facilitates convergence.

The optimization takes an iterative approach and progressively removes elements by ranking their associated sensitivity number. Before reaching the target volume fraction, the number of elements removed in each iteration is controlled by the evolutionary volume ratio ER. The evolution of the volume can be expressed by:

$$V_{m+1} = V_m(1 - ER) \quad (m = 1, 2, 3, \cdots) \tag{8}$$

Once the target volume constraint is met, the volume of the structure will be kept constant as V^* for the remaining iterations. The ratio between the prescribed target volume and the

initial volume of the structure is termed volume fraction (VF). Sensitivity ranking is based on the Optimality Criteria (OC). The optimization is deemed convergent if the variation of the objective function during the last ten iterations is lower than a prescribed convergence threshold. For more details on the BESO formulation, interested readers should refer to the book by Huang and Xie [77].

3.2. Self-support constraint

During the process of 3DCP, the ability to remain self-supporting is a governing criterion when assessing buildability. The quality of being self-supporting depends on various factors, including the material composition, printer specification, printing environment, and the structure's geometry. Unlike small-scale AM, such as FDM, 3DCP is generally subject to a much stricter overhang limit of 70° to 90°, where vertical alignment (90° overhang) is commonly observed [38,48–51]. In this work, it is conservatively assumed that the self-supporting overhang angle is 90°; in other words, each newly printed layer should be supported vertically by the previously fabricated layer. This conservative assumption is based on the following reasons:

- Although printers and materials have witnessed continuous improvement, many 3DCP practices still prefer vertical alignment to maintain structural stability.
- Designs that allow a less strict overhang constraint tend to create separated regions at a lower volume fraction. In order to achieve geometrical continuity, such designs require many structural elements to be reconnected. Having too many connection routes may lower the overall structural efficiency.
- The geometrical simplicity of vertical alignment allows it to be compatible with other constraints and increases the overall computational efficiency.

To symbolize this feature in topology optimization, a layer-wise sensitivity scheme is formulated to mimic the physical supporting condition.

The cuboid design domain is firstly discretized into $n_x \times n_y \times n_z$ uniformly spaced elements. While all principal axes can be specified as the print direction, the positive Z-axis is chosen in this section for ease of explanation. Each layer of elements in the XY plane can then be assumed as a physical layer to be printed. Consequently, if all elements in the design domain (except the first layer to be supported by the baseplate) have a solid element beneath it, the optimized design achieves self-support. As the evolution in conventional BESO is controlled by ranking element sensitivity, element addition and removal are based on the structural significance. In the proposed layer-wise sensitivity scheme, we modify the sensitivity number to emphasize the importance of the geometric constraint as follows:

$$\alpha^*_{i,j,k} = \alpha_{i,j,k} + \sum_{k}^{n_z} \alpha_{i,j,k+1}\beta_{i,j,k+1} + \alpha_{i,j,k+2}\beta_{i,j,k+2} + \cdots + \alpha_{i,j,n_z}\beta_{i,j,n_z} \tag{9}$$

Where i, j, k denote the index on the principal axes, n_z is the total number of elements on the z-axis, $\alpha^*_{i,j,k}$ is the modified sensitivity number and the value of $\beta_{i,j,k}$ depends on the element state $\rho_{i,j,k}$:

$$\beta_{i,j,k} = \begin{cases} 1 & when \ \ \rho_{i,j,k} = 1 \\ \beta_{min} & when \ \ \rho_{i,j,k} = \rho_{min} \end{cases} \tag{10}$$

where β_{min} is specified as 10^{-9} to minimize the contribution of void elements.

Mathematically speaking, the modified sensitivity number of an element is the sum of the sensitivity numbers of all solid elements above it in the printing direction. This expression means that, in the element update scheme, the sensitivity of lower elements simultaneously considers the structural contribution of upper elements. Analogous to the physical printing

process, the significance of lower elements is emphasized as the removal of lower parts will inevitably cause the upper structure to collapse. With the layer-wise sensitivity scheme, element update takes a top-down approach, and element addition/removal begins from the upper surface of the current design. As the layer-wise sensitivity scheme is a global function and can be efficiently computed based on matrix operation, the extra computational time of this step is negligible compared with the FEA time. It is also worth noting that the layer-wise sensitivity scheme should be carried out after the filter scheme and history averaging scheme; otherwise, the vertical continuity may not be strictly guaranteed.

3.3. Continuous extrusion constraint

To prevent the build-up of pressure within the nozzle and improve print quality, the capability of continuous extrusion is another desirable quality for 3DCP. In order to enable continuous extrusion, continuity needs to be guaranteed on two levels: a single connected and enclosed 2D shape in each sliced layer and a continuous toolpath to fill each 2D shape. This subsection introduces a continuous extrusion constraint in the topology optimization framework to generate connected and enclosed 2D geometry in each layer. This proposed strategy can be used in conjunction with the authors' work on generating a continuous toolpath [78] to achieve the global continuity of an optimized design.

Like the self-support constraint, each horizontal layer of the design domain is assumed to be a physical layer for fabrication. The complex geometrical problem is then simplified from 3D to 2D, where the objective is to ensure the solid elements within each 2D layer form an interconnected region. In order to be compatible with the self-support constraint, the continuous extrusion constraint takes a bottom-up approach, and the examination starts from the lower layers towards the upper layers; this ensures that each interconnected region can be supported by the layer beneath it.

With i, j, k representing the index of an element on the principal axes, let l_k^m denote the kth layer measured in the print direction at the mth iteration. With a bottom-up approach, the search starts from l_1^m and move upwards. The first step is to check if all solid elements on l_k^m can form an interconnected region. With binary design variable in BESO, each 2D layer can be treated as a binary image, and the problem can be solved using the connected component labeling algorithm. Fig. 1 illustrates the concept of the connected component labeling algorithm of a 2D binary image. Starting in the top left corner, a recursive search is circulated through the binary image to check and label connected components. With 4-neighbors as connectivity, each element $e_{i,j,k}$ can be associated with four adjacent pixels ($e_{i-1,j,k}, e_{i+1,j,k}, e_{i,j-1,k}, e_{i,j+1,k}$) on the same layer for a possible connection. It should be noted that four neighbors in the diagonal position are ignored in this case. In Fig. 1b, there are four isolated components. For more details on the theoretical background and implementation of the connected component labeling algorithm, interested readers should refer to a recent review on this topic [79]. In the Python platform, an efficient connected component labeling algorithm is available in the Scikit-image library, which is programmed based on works in the literature [80,81]. After performing the search, if the number of labeled components is one (the number of the enclosed region $g_k = 1$), all elements are clustered into an interconnected region, and the continuous extrusion constraint is satisfied in this layer; Contrarily, if the number is larger than one (the number of the enclosed region $g_k > 1$), the shortest possible routes should be located to reconnect the isolated regions using the following steps.

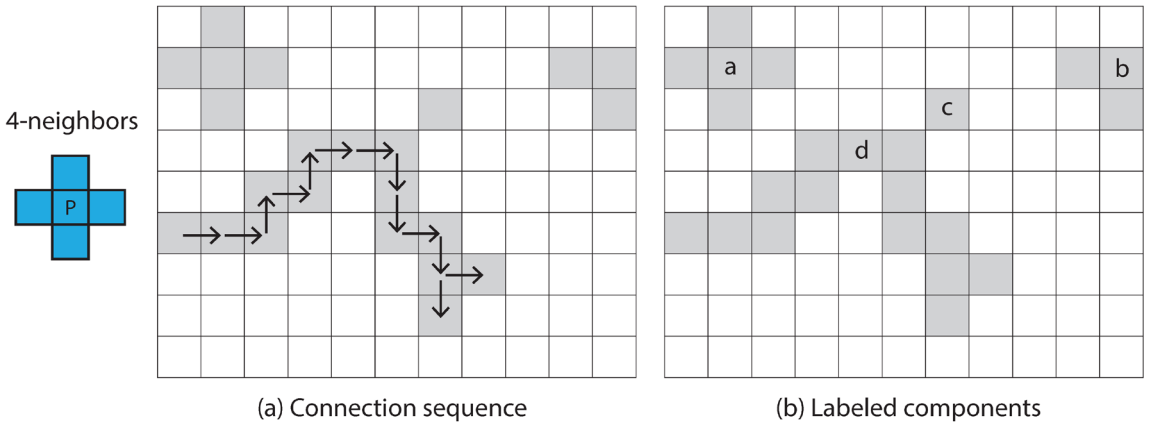

Fig. 1. Illustration of the connected component labeling algorithm. (a) the connection sequence is from left to right and then top to bottom. (b) with 4-neighbors as connectivity, four separate components are labeled in this example.

Suppose that l_k^m has isolated regions, the second step is to identify potential areas suitable for reconnection. Such areas should meet three criteria: (1) elements in this region should be supported by the layer below; (2) elements in this region should be of structural importance; (3) the region should cover the shortest possible route. In this regard, the potential area for reconnection R is determined as:

$$R = \left\{ e_{i,j,k} \,\middle|\, \rho_{i,j,k-1}^m = 1 \text{ and } \rho_{i,j,k}^{m-1} = 1 \text{ and } \rho_{i,j,k}^m = \rho_{min} \right\}, \tag{11}$$

where $\rho_{i,j,k}^m$ denote the design variable of an element with a coordinate i, j, k at the mth iteration and ρ_{min} is the design variable of a void element. The expression identifies elements under two conditions: (1) the elements are supported by solid elements below in the current iteration; (2) the elements are solid in the previous iteration and removed in the current iteration. The first condition meets the self-support constraint, thereby preventing the formation of an overhang. As element update is achieved by ranking the sensitivity, elements removed in the previous iteration (m-1) have better performance than elements deleted in prior iterations

(1, 2, ..., m-2). The algorithm selects elements in the previous iteration to ensure that the added elements are marginally competitive in structural performance.

Fig. 2 illustrates how R can be found by overlapping the two conditions.

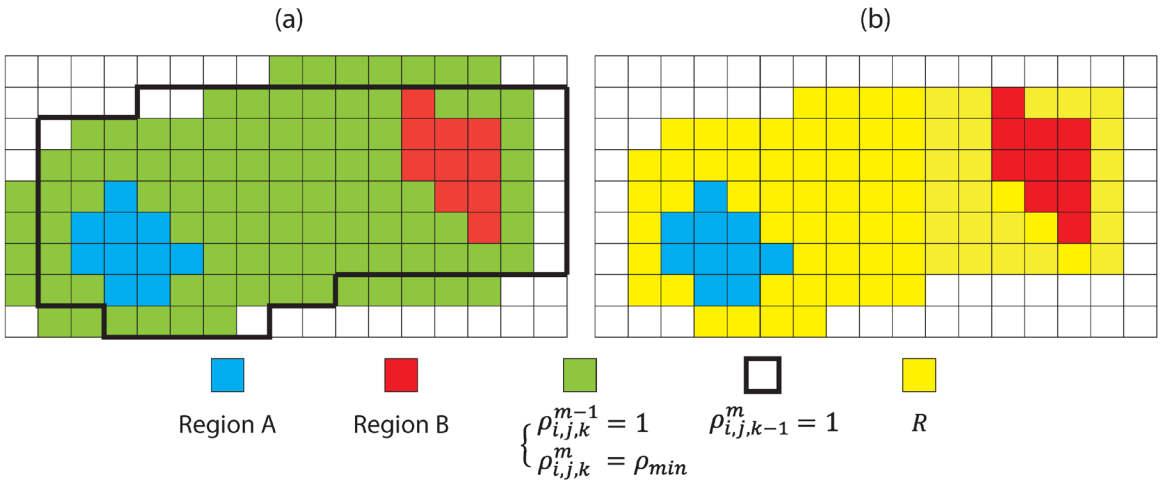

Fig. 2. Demonstration of how the potential area for reconnection R is found between 2 isolated regions, A and B: (a) Elements within the thick black line represent the solid elements in the layer below, while green elements are elements removed in the current iteration; (b) By overlapping the two conditions, the yellow elements are potential candidates to be added back to link the isolated regions.

Once R is located, the next step is to find the shortest possible route based on a minimum distance principle. With an isolated region as the center, its distance to all elements in R is measured based on 4-neighbors connectivity. The calculation is similar to the dilation method commonly used in image processing applications. The process is iterated until the distance values of all elements within R are determined; the result is termed the distance map in this section. By summing the distance maps between a pair of isolated regions, the elements with the lowest summed value form the shortest possible route. Fig. 3 illustrates how the shortest possible route is established using the minimum distance principle. In rare cases where the connection path is curvy, adding elements with a single minimum value (10 in Fig. 3) may not link two isolated regions; elements with larger distance values are added (11, 12 ⋯) until the connection is restored. When multiple islands are present in a layer, the connection follows the same principle by locating the shortest possible route between pairs of isolated regions one by one,

prioritizing the closest pairs. Fig. 4 demonstrates how multiple isolated regions in Fig. 1 can be connected using the proposed algorithm. The yellow and orange regions (C and D) form the closest pair and are connected first (Fig. 4a). Subsequently, the second closest region in blue (A) is connected by adding elements with the summed distance of two and three (Fig. 4b). Finally, the connection path between the red (B) and the newly merged orange region (C) is created by adding elements with a summed distance of four. After connections, all isolated regions are joined into an enclosed area.

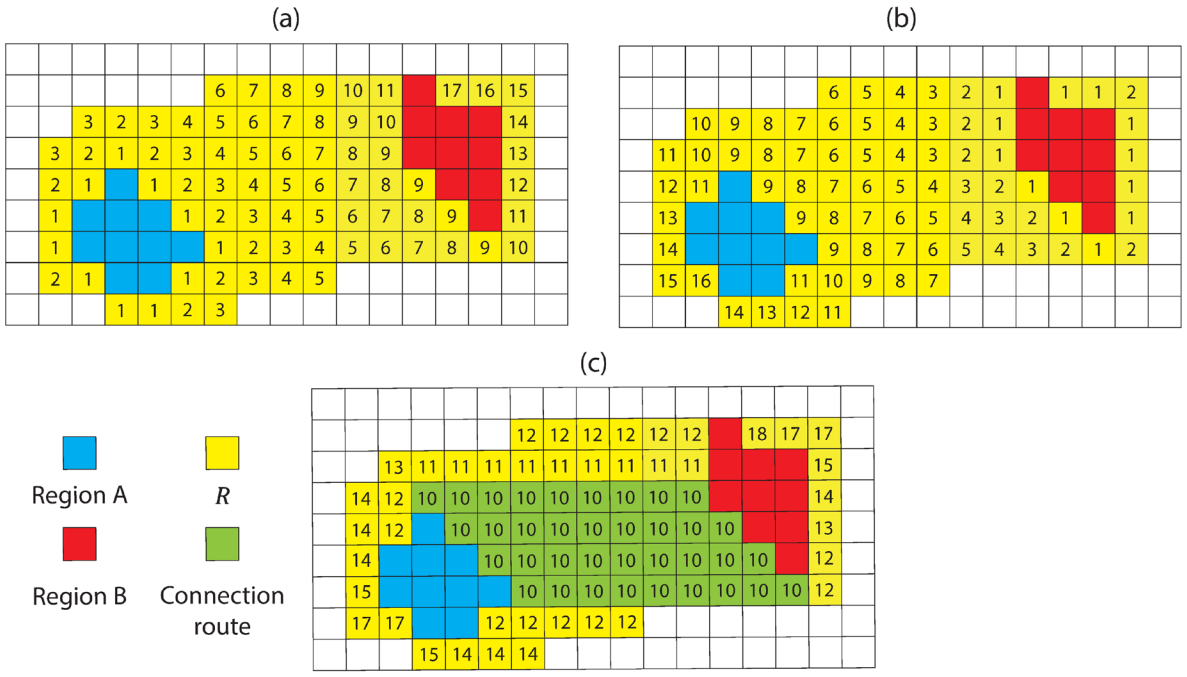

Fig. 3. Demonstration of how the shortest possible route is found within the potential area for reconnection: (a) the distance map of region A; (b) the distance map of region B; (c) the sum of the two distance maps; the shortest connection route is located by adding elements with the lowest summed distance value.

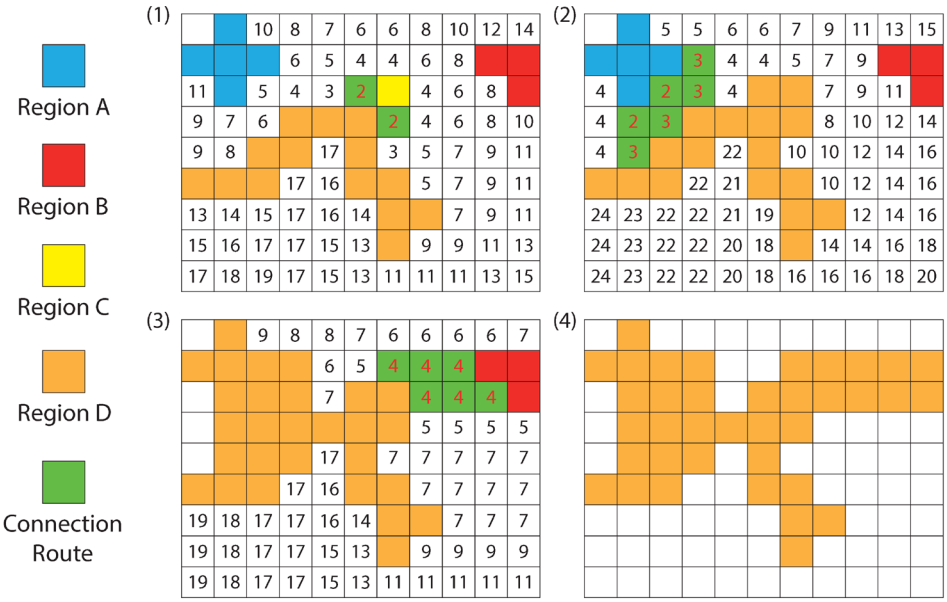

Fig. 4. Illustration of how four isolated regions are connected using the proposed algorithm. Elements with the lowest summed distance (green) become the connection routes: (1) Regions C and D form the closest pair and are connected first; (2) Elements with the summed distance of two and three become the connection path between regions A and D; (3) With the largest distance between regions, the connection between regions B and D becomes the last step; (4) The enclosed region after reconnection.

Adding elements for reconnection will inevitably violate the volume constraint in the current iteration; therefore, an equal number of elements need to be removed. As the Optimality Criteria remove elements with the lowest sensitivity values, the elements on the connection route may be deleted again during this process. In order to prevent the loss of connection in future iterations, each added element is assigned a unique factor $\lambda_{i,j,k}$ to scale up its sensitivity. The value of $\lambda_{i,j,k}$ is initialized as one; every time the added element is deleted during the element update scheme, its $\lambda_{i,j,k}$ is multiplied by two. The search for a suitable $\lambda_{i,j,k}$ for each added element will be repeated until all added elements can be preserved during the element update process. In the next iteration, the global matrix of $\lambda_{i,j,k}$ is inherited but multiplied by a factor of 0.9 to soften its presence in future iterations.

3.4. Domain segmentation for modular construction

To bypass the overhang limit, many applications of 3DCP split a structure into segments, which are fabricated separately and assembled subsequently. Each segment can be positioned in its favorable orientation to maximize the self-supporting capability. Work in the literature [37] adopts a post-processing strategy, where a structure is segmented after the topology optimization process. Such a strategy necessitates careful design considerations and potentially the need for significant geometrical modifications or excessive subdivisions. In this subsection, a different approach is proposed by integrating the concept of modular construction within the topology optimization framework. Compared with the post-processing method, specifying segments explicitly within the topology optimization framework shows two advantages: (1) the form-finding process ensures the structural performance of each segment; (2) each segment can strictly follow the self-support and continuous extrusion constraints.

With a uniformly spaced mesh grid, the design domain can be constructed as a 3D matrix, with each element characterized by its unique index in the principal axes. The global 3D matrix can then be disassembled into smaller subdomains for domain segmentation. The number and size of the subdomains are user-defined prior to the topology optimization process. Compatible with the self-support and continuous extrusion constraints, each subdomain is assigned its specific print direction. During the optimization process, the layer-wise sensitivity scheme for the self-support constraint is operated separately in each subdomain. The global sensitivity matrix is later obtained by assembling the individual matrix of the subdomains. Similarly, the continuous extrusion constraint is carried out in each subdomain to ensure the geometrical continuity of each segment. Fig. 5 illustrates how a cuboid design domain is subdivided into three distinct segments whose print directions are dissimilar. Intuitively, designs created using this method directly depend on the selection of domains and printing orientations. The strategies for domain segmentation fall into two categories: dimension-orientated and

performance-orientated. Firstly, when the design dimension exceeds the printer's limit, the design domain can be partitioned so that each segment can fit within the workspace. Secondly, the designer can first carry out an FEA or topology optimization to identify the critical structural path. The domains and printing orientations can be chosen to align with such structural paths, thereby maximizing the structural performance. Normally, the surface with the largest area is a good choice for the printing baseplate. The interface between domains can often be positioned at the mirror plane when the design has a symmetrical boundary condition. It is worth noting that the assembly of the segments is essential to enhancing the structure's strength and stability and should be carefully designed after the optimization process. Potential assembly strategies include chemical bonding using adhesives, casting concrete near contact surfaces, and post-tensioning and grouting in preassigned tunnels.

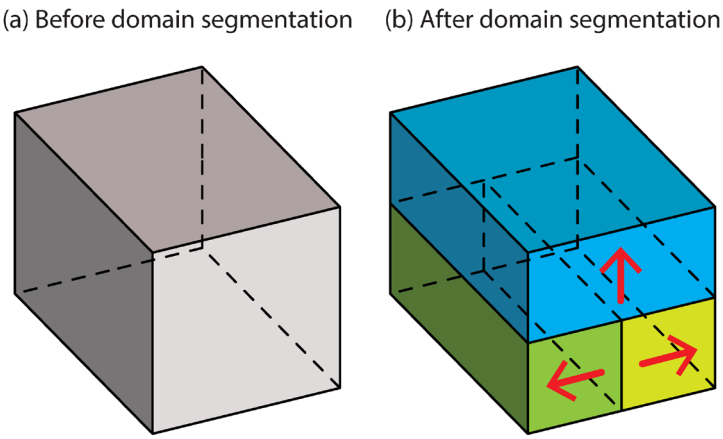

Fig. 5. Illustration of the concept of domain segmentation. After subdividing the design domain, each segment can be assigned a specific print direction.

3.5. Anisotropy in 3DCP

Because of the nature of layer-wise fabrication, the outcome of 3DCP commonly exhibits anisotropic behaviors. Work in the literature [31,32,52] reports that the interface between vertical layers tends to be the structure's weak spot, resulting in a lower bonding strength in the vertical plane than in the horizontal plane. Depending on the toolpath alignment and infill

quality, the structure may also be anisotropic in the horizontal plane. In this subsection, we simplify the problem by assuming the material of 3DCP to be transverse isotropic. In other words, the material on the horizontal plane is assumed to be homogenous, whereas the vertical strength differs. For the transverse isotropic model, the material's orientation needs to be defined in FEA to distinguish the vertical and horizontal planes. In this section, the homogeneous horizontal plane is denoted as the XY plane, as opposed to the vertical Z-axis. For different manufacturing directions, the orientation of the material should be adjusted accordingly to match the planes. The transformation of a cuboid design domain can be done by rotating the principal axes at 90°.

In 3D, the element stiffness matrix $\boldsymbol{K^0_{i,j,k}}$ is integrated over element volume V_e as:

$$\boldsymbol{K^0_{i,j,k}} = \int_{V_e} \boldsymbol{B^T}\, \boldsymbol{C^0_{i,j,k}} \boldsymbol{B}\ dV \tag{12}$$

where $\boldsymbol{B}$ is the strain-displacement matrix and $\boldsymbol{C^0_{i,j,k}}$ is the stiffness matrix derived from Hooke's Law. The stiffness matrix $\boldsymbol{C^0_{i,j,k}}$ can be found from the inverse of the compliance matrix, which is formulated as:

$$\begin{bmatrix} \varepsilon_{xx} \\ \varepsilon_{yy} \\ \varepsilon_{zz} \\ \varepsilon_{yz} \\ \varepsilon_{zx} \\ \varepsilon_{xy} \end{bmatrix} = \begin{bmatrix} \frac{1}{E_x} & -\frac{v_{yx}}{E_y} & -\frac{v_{zx}}{E_z} & 0 & 0 & 0 \\ -\frac{v_{xy}}{E_x} & \frac{1}{E_y} & -\frac{v_{zy}}{E_z} & 0 & 0 & 0 \\ -\frac{v_{xz}}{E_x} & -\frac{v_{yz}}{E_y} & \frac{1}{E_z} & 0 & 0 & 0 \\ 0 & 0 & 0 & \frac{1}{G_{yz}} & 0 & 0 \\ 0 & 0 & 0 & 0 & \frac{1}{G_{zx}} & 0 \\ 0 & 0 & 0 & 0 & 0 & \frac{1}{G_{xy}} \end{bmatrix} \begin{bmatrix} \sigma_{xx} \\ \sigma_{yy} \\ \sigma_{zz} \\ \sigma_{yz} \\ \sigma_{zx} \\ \sigma_{xy} \end{bmatrix} \tag{13}$$

where E, v, and G are the Young's modulus, Poisson's ratio, and shear modulus in the corresponding directions. For transverse isotropic material, the material is assumed to be homogenous in the XY plane, and the compliance matrix is simplified as:

$$\begin{bmatrix} \varepsilon_{xx} \\ \varepsilon_{yy} \\ \varepsilon_{zz} \\ \varepsilon_{yz} \\ \varepsilon_{zx} \\ \varepsilon_{xy} \end{bmatrix} = \begin{bmatrix} \frac{1}{E_p} & -\frac{v_p}{E_p} & -\frac{v_{zp}}{E_z} & 0 & 0 & 0 \\ -\frac{v_p}{E_p} & \frac{1}{E_p} & -\frac{v_{zp}}{E_z} & 0 & 0 & 0 \\ -\frac{v_{pz}}{E_z} & -\frac{v_{pz}}{E_p} & \frac{1}{E_z} & 0 & 0 & 0 \\ 0 & 0 & 0 & \frac{1}{G_{zp}} & 0 & 0 \\ 0 & 0 & 0 & 0 & \frac{1}{G_{zp}} & 0 \\ 0 & 0 & 0 & 0 & 0 & \frac{2(1+v_p)}{E_p} \end{bmatrix} \begin{bmatrix} \sigma_{xx} \\ \sigma_{yy} \\ \sigma_{zz} \\ \sigma_{yz} \\ \sigma_{zx} \\ \sigma_{xy} \end{bmatrix} \quad (14)$$

where E_p and v_p are the Young's modulus and Poisson's ratio in the XY plane, E_z, v_{zp}, and G_{zp} are the Young's modulus, Poisson's ratio, and the shear modulus in the Z direction. After conducting lab tests, the five engineering constants can be specified in the FEA analysis and influence the topology optimization process. It should be noted that both the compliance matrix and stiffness matrix comprise only constants, which do not affect the derivation of the objective function in topology optimization.

3.6. Workflow of the proposed framework

With four manufacturing constraints considered, the workflow of the proposed topology optimization framework is illustrated as a flowchart in Fig. 6.

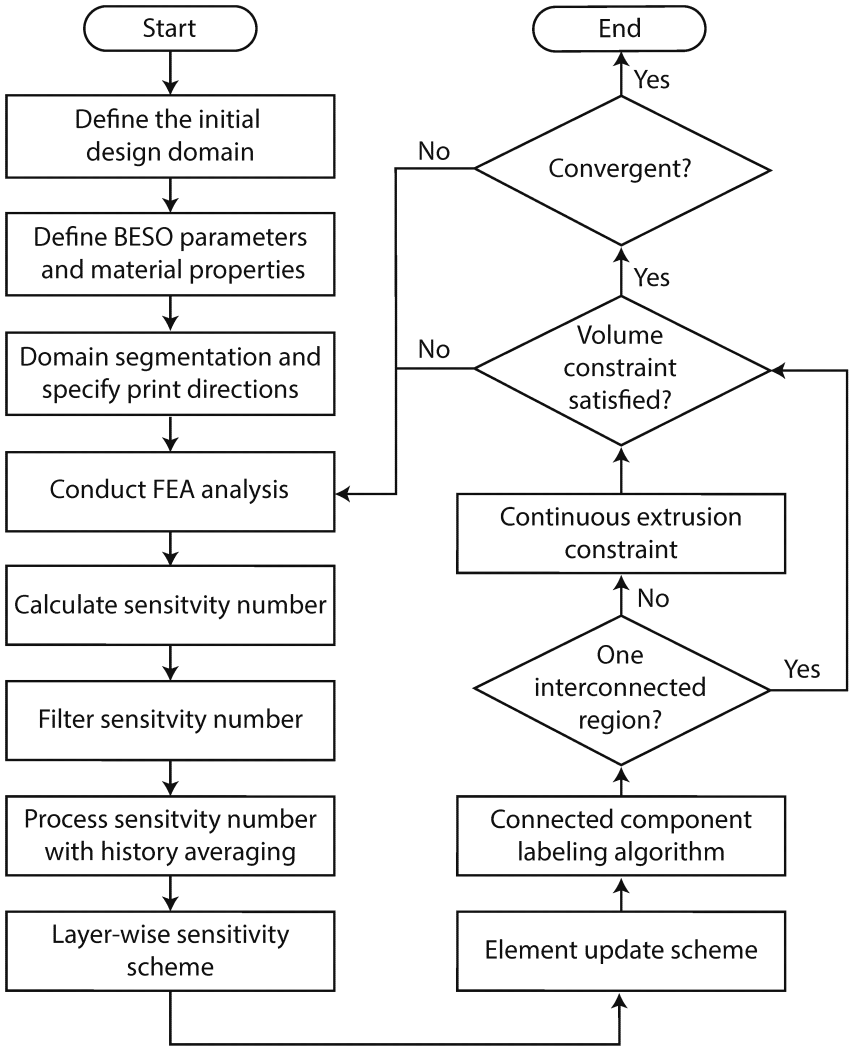

Fig. 6. Flowchart showing the implementation of the proposed strategy.

4. Numerical studies

Thie section aims to test the robustness and effectiveness of the proposed algorithm based on the benchmark cantilever example widely used in topology optimization studies. Each subsection exemplifies how different manufacturing constraints are reflected in the topology optimized designs. Sufficient iterations are performed until the prescribed convergence threshold, defined as the variation of the objective function during the last ten iterations, is below 0.1%. For visualization, the optimized results are smoothed using Laplacian smoothing in the Rhino and Grasshopper platform. Same viewpoints are maintained for the examples to

ensure consistency. The optimization is implemented in the Python platform on an 8-cores Intel ® i7-9700K CPU 3.60Hz with 32GB RAM.

As shown in Fig. 7, the design domain of the cantilever structure has a dimension of $180\ \text{mm} \times 60\ \text{mm} \times 60\ \text{mm}$. With a grid size of $1\ \text{mm}$, the design domain is discretized into fine mesh with $648{,}000$ elements. One end has a fixed boundary condition, while a load of 100 N is uniformly distributed on a 3 mm wide area at the other end. The material properties reported in previous work [82] are used, with the Young's modulus as 21.9 GPa, Poisson's ratio as 0.2, and Shear modulus as 9.1 GPa. The Young's modulus for void elements is specified as 10^{-9} GPa and the binary design variable for solid and void elements are 1 and 0.001, respectively. To circumvent the checkerboard problem, a consistent filter radius of $5\ \text{mm}$ is adopted. The evolutionary ratio and volume fraction are prescribed as 1% and 50% for all examples.

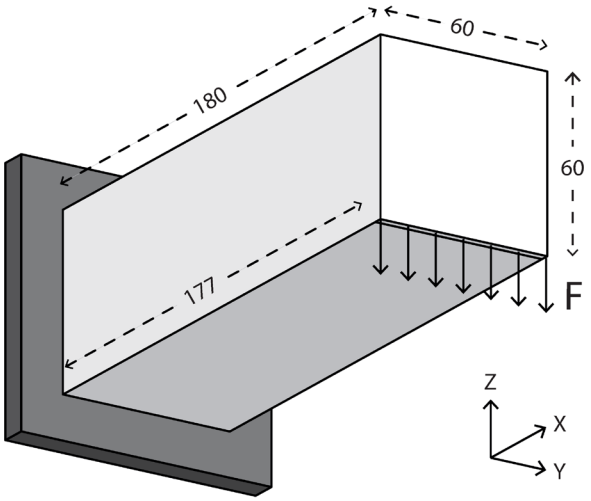

Fig. 7. Boundary and loading conditions of the cantilever structure.

4.1. Self-support constraint

This subsection shows the optimized designs with the self-support constraint under different print directions. Both the front and rear views are presented to maximize the

visualized details. Note that the illustrated principal axes in the figures should match with the front and rear views accordingly.

Fig. 8a shows the original BESO design without the self-support constraint, whose compliance is 3541.5. This original design and its compliance are used as the benchmark to be compared with other results in this section. The geometry of the original BESO design is characterized by the top and bottom flanges, which are in tension and compression, respectively. The coupling of the two flanges forms an efficient load path. Fig. 8b illustrates the design when printing towards the negative Y-axis. The outer parts, including the loading zone near the free end and the two flanges, remain basically unchanged. However, the middle part between the flanges is reshaped to become self-supporting. The result printing towards the positive Y-axis shows the same design because of symmetry and is therefore omitted here. When printing towards the positive X-axis (Fig. 8c), the top flange is removed in the design, and more structural volume is allocated in the middle part. Both flanges are kept in the design when printing towards the negative X-axis. Although the top flange near the free end may be structurally inferior, it is preserved as the base to support the upper part along the print direction. When printing along the Z-axis (Fig. 8e and f), more structural volume and associated loading paths are aligned in the Z direction. The volume on the top flange (Fig. 8e) and bottom flange (Fig. 8f) are partly removed to satisfy the self-support constraint. However, as suggested by the predominant presence of vertical elements, the 90° overhang constraint has imposed a strong geometry limitation; this observation is particularly evident in Fig. 8e and f, which has a nearly solid solution in the z-direction. In some cases, such strict restrictions may deviate the design from the optimum solution and limit the design freedom. A less strict overhang angle constraint should be developed in future work for 3DCP printers capable of creating overhanging features.

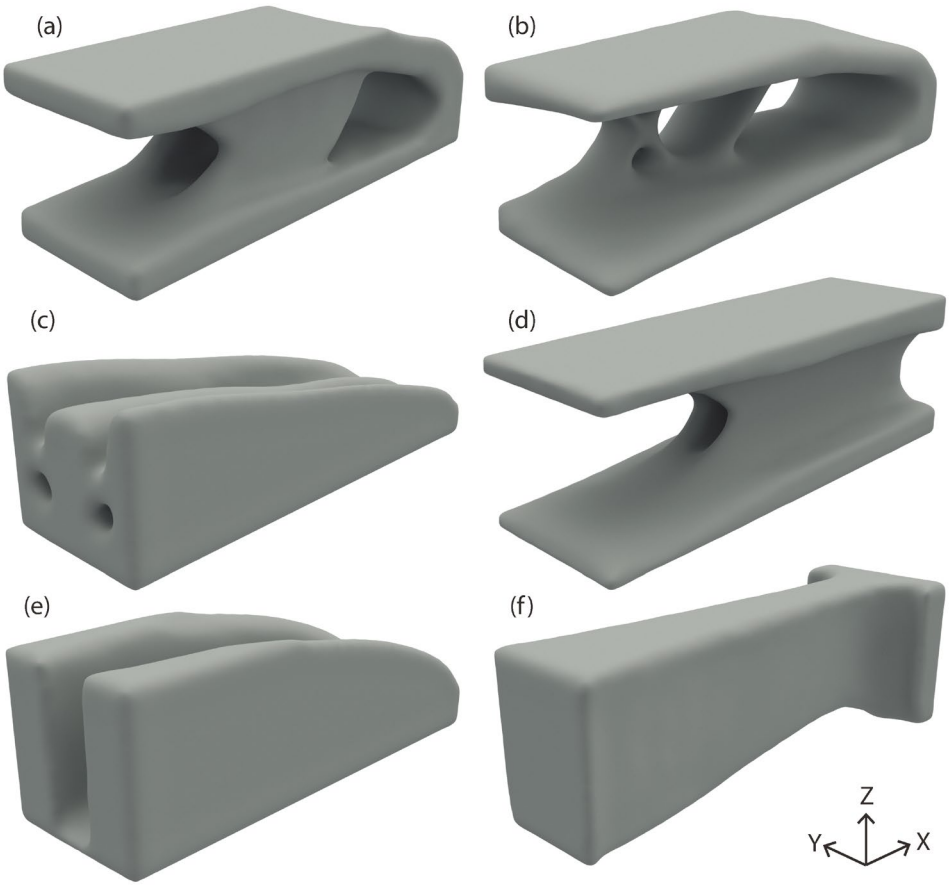

Fig. 8. Rear views of designs under different print directions: (a) original BESO design; (b) towards positive Y-axis; (c) towards positive X-axis; (d) towards negative X-axis; (e) towards positive Z-axis; (f) towards negative Z-axis.

Table 1 summarizes the compliance of the designs under different print directions. With great similarity to the original BESO result, the design with a negative Y print direction has a negligible increase of 0.4% in compliance. A slight increase of 2.3% in compliance is observed for the negative X printing direction; the structural performance is maintained by keeping both the top and bottom flanges in this case. By comparison, the other three cases have a moderate increase from 5.4% to 14.9% in compliance. The relatively worse stiffness of those three designs is caused by removing elements on the top or bottom flanges to meet the self-support constraint. Overall, the increase in compliance in all cases is within an acceptable range and is justifiable given the strict overhang requirement.

Table 1. The comparison of the designs' compliance values under different print directions.

	Original	Negative Y	Positive X	Negative X	Positive Z	Negative Z
Compliance	3541.5	3556.5	4069.6	3623.1	3733.5	3811.0
Normalized percentage (%)	100.0	100.4	114.9	102.3	105.4	107.6

4.2. Continuous extrusion constraint

This subsection demonstrates how the continuous extrusion constraint can be implemented on top of the self-support constraint. In section 4.1, the last three designs fail to form an interconnected region in some layers (Fig. 8d, e, and f), preventing a continuous printing operation. In Fig. 8d, the top and bottom flanges are disconnected near the fixed boundary, creating two isolated regions in each layer. By introducing the continuous extrusion constraint, a continuous path along the Z direction is formed to link the flanges (Fig. 9a). The reshaped design resembles an I-shaped beam commonly found in cantilever structures. When printing towards the positive Z-axis (Fig. 8e), the two thick walls on two sides of the Y-axis are disconnected. To form a connection on each layer, a thin wall is added near the fixed boundary (Fig. 9b). The location of this connection path is structurally important as more stress is concentrated near the clamped end. In the last example (Fig. 9c), more elements are added to the bottom flange to refill the disconnected bottom part in Fig. 8f.

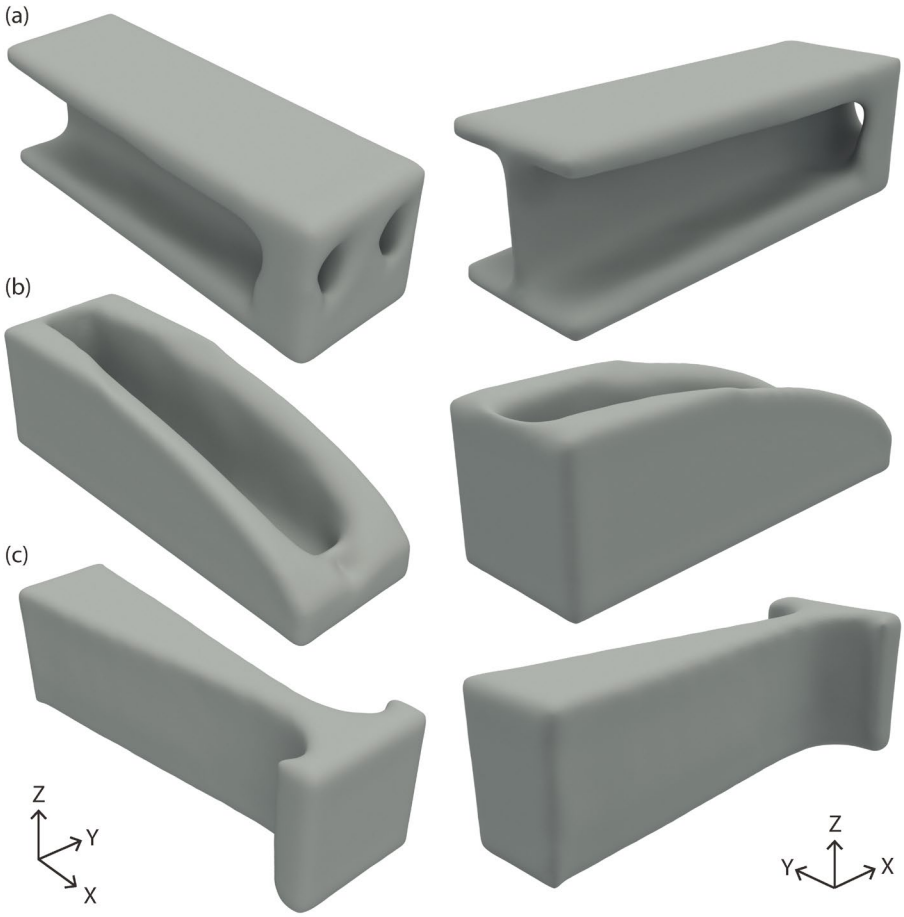

Fig. 9. Self-supporting designs with continuous extrusion constraint under different directions: (a) towards negative X-axis; (b) towards positive Z-axis; (c) towards negative Z-axis.

Table 2 compares the compliance of the designs with and without the continuous extrusion constraint (continuous extrusion is noted as CE in the table). The first two results (negative X and positive Z) show a slight increase in compliance by 0.8% and 1.9%, respectively; this is caused by relocating the elements from structurally significant areas to form the connection path. However, since the algorithm can determine the shortest possible route with structural importance, the increase in overall compliance is within an acceptable range. Interestingly, the compliance in the last example with the continuous extrusion constraint is even 2.4% lower, which again emphasizes the structural contribution of the bottom flange. In summary, the continuous extrusion constraint can successfully link isolated areas in each layer without significantly affecting the structural performance of the designs.

Table 2. The comparison of the designs' compliance values with and without the continuous extrusion (CE) constraint.

	Original	Negative X	Negative X (CE)	Positive Z	Positive Z (CE)	Negative Z	Negative Z (CE)
Compliance	3541.5	3623.1	3654.3	3733.5	3798.4	3811.0	3726.0
Normalized percentage (%)	100.0	102.3	103.1	105.4	107.3	107.6	105.2

4.3. Modular construction

On top of the previous two manufacturing constraints, the feature of domain segmentation is evaluated in this subsection. Two modular design prototypes are presented by allowing two subdomains in the Y-axis, with opposite print directions in each segment. Modular design A (Fig. 10a) places the base plate in the middle section and prints towards the cantilever's two sides along the Y-axis. The resulting design shares great similarities with the original design. Modular design B (Fig. 10b) relies on the same two subdomains, but the print directions are from the sides towards the middle section. As a result, the vertical members linking the two flanges are now shifted from the middle section to the sides, allowing self-support in each segment. In terms of compliance, both designs match the original design, providing competitive alternative solutions.

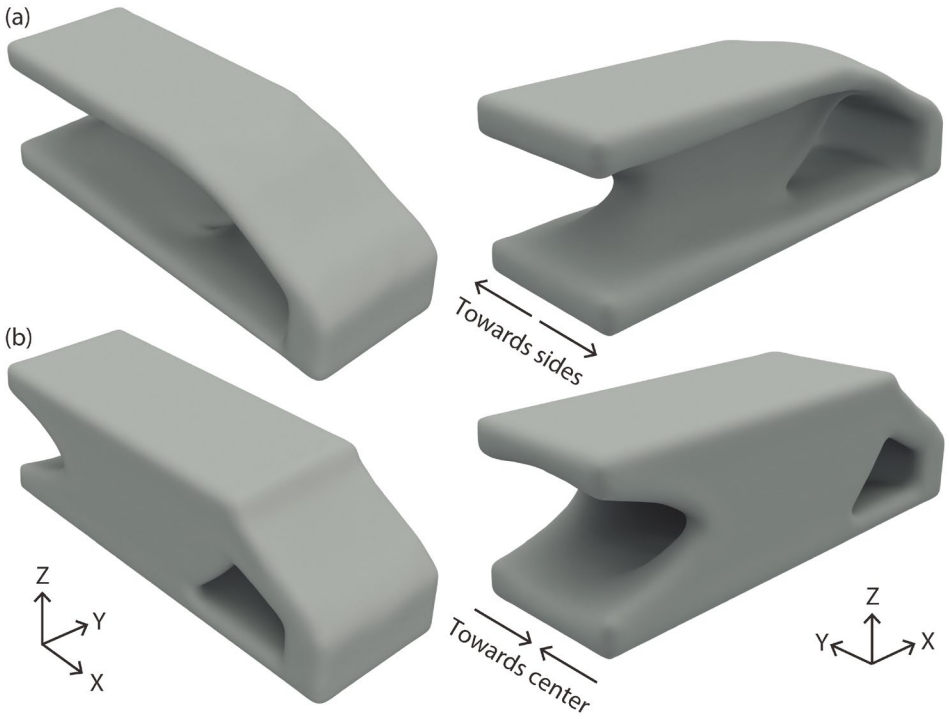

Fig. 10. Modular designs: (a) design A: printing towards the sides of the Y-axis; (b) design B: printing towards the centerline of the Y-axis.

Table 3. The comparison of the modular designs' compliance values.

	Original	Modular design A	Modular design B
Compliance	3541.5	3542.1	3544.4
Normalized percentage (%)	100.0	100.0	100.0

To simulate the physical printing result, the two modular designs are sliced and filled with continuous toolpaths based on the authors' previous work [78]. As shown in Fig. 11, each printed layer can form an interconnected 2D region and support the successive layer. Combining the continuous extrusion constraint with the continuous toolpath algorithm allows a topology optimized design to be fabricated, achieving good print quality and efficiency.

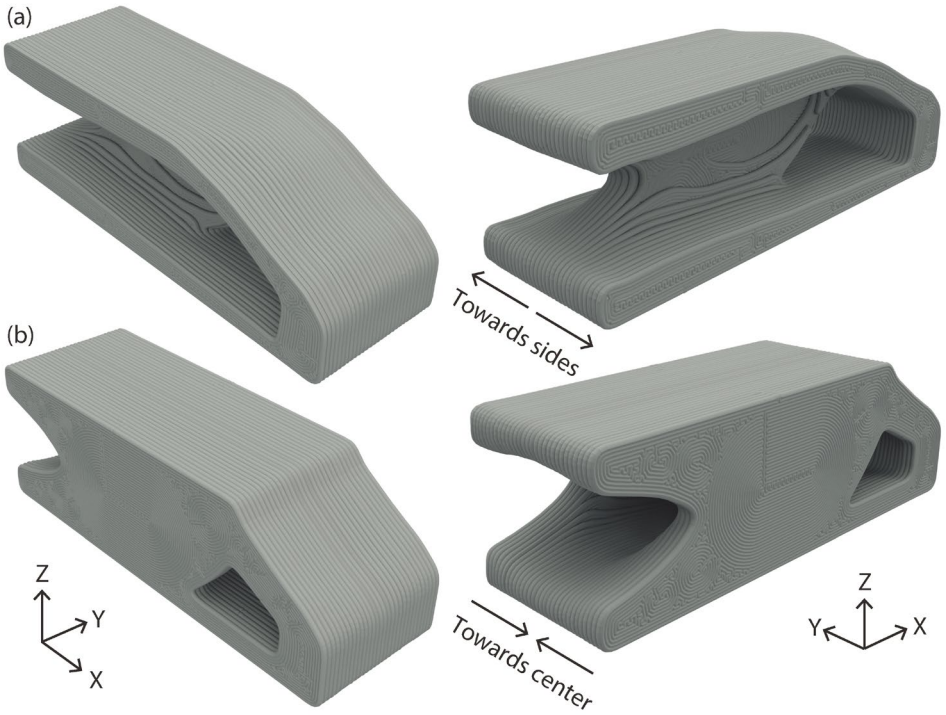

Fig. 11. Simulated printing result for the modular designs including sliced layers and continuous toolpaths: (a) design A; (b) design B.

4.4. Anisotropy in 3DCP

The subsection tests how the anisotropy of 3DCP can affect the topology optimized designs. For simplification, all other material properties are kept constant except for the Young's modulus in the print direction. The compliance values of different designs are not comparable as the material properties differ. Two examples are tested under the negative Y print direction with the continuous extrusion constraint; reduction factors of 0.5 and 0.1 are assigned to the Young's modulus in the two designs.

The generated designs are shown in Fig. 12. By comparison, the outer profile, including the flanges and the loading area, remains similar, but the load paths between the flanges have seen noticeable changes. With a lower Young's modulus in the print direction, less structural volume is allocated on the middle loading frames, and more volume is repositioned onto the flanges. The change in geometry can be attributed to two reasons: (1) the change in material properties

affects the global sensitivity matrix in each iteration, leading to different optimization paths; (2) with a lower Young's modulus in the print direction, more structural volume is effectively relocated onto the horizontal plane to increase overall stiffness. To sum up, allowing anisotropy can lead to different optimized designs, but the main structural elements remain similar.

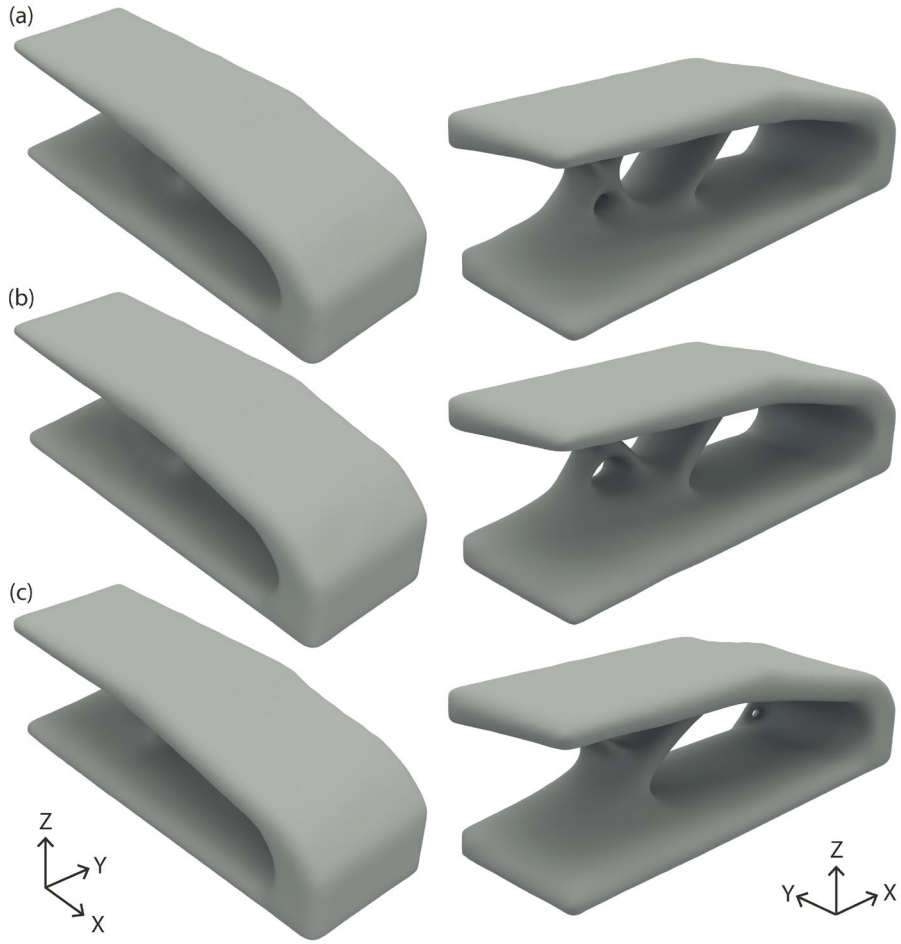

Fig. 12. Optimized designs with different Young's modulus on the Y direction: (a) Ey = E; (b) Ey = 0.5E; (c) Ey = 0.1E.

4.5. Computational efficiency

This subsection evaluates the proposed algorithm's computational efficiency and iteration history based on modular designs A and B presented in Section 4.3. As shown in Fig. 13, both modular designs have a stable iteration history, with a steady increase in compliance before convergence. Inefficient elements are progressively removed during the iteration process.

Table 4 summarizes the computational time of both designs compared with the original BESO design. The additional computational time by adding the manufacturing constraints, as 2.1% and 3.1%, is negligible compared to the FEA time. Therefore, the proposed framework is comparable to the original BESO framework in computational efficiency and stability.

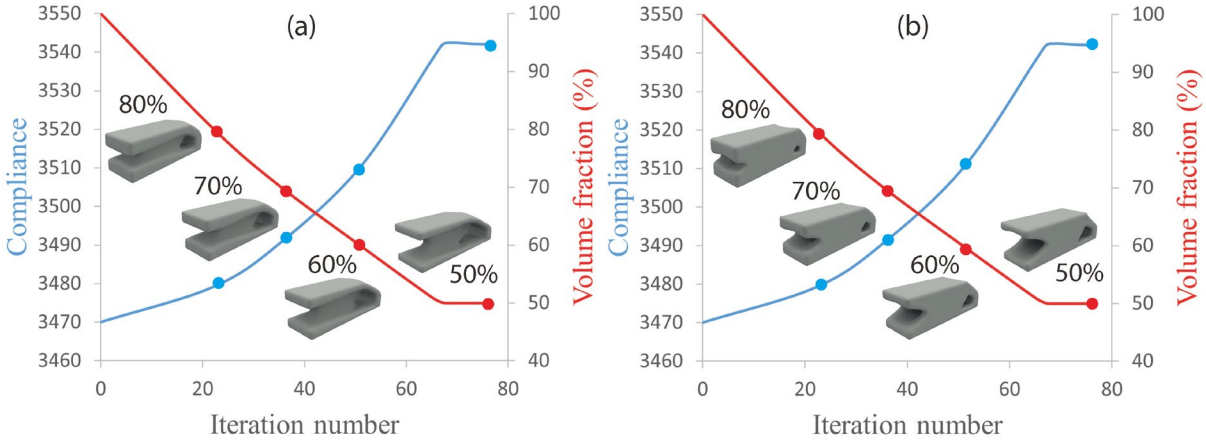

Fig. 13. Iteration history for two modular designs: (a) design A; (b) design B.

Table 4. The comparison of the computational time of different modular designs.

	Original	Modular design A	Modular design B
Computational time (min)	1442	1473	1487
Normalized percentage (%)	100.0	102.1	103.1

4.6. Designs under low volume fractions

This subsection tests the algorithm's robustness under low volume fractions. As shown in Fig. 14, optimization of modular design A can converge at three low volume fractions: 30%, 20%, and 10%. By comparison, ineffective structural volumes are gradually removed until a slender design is reached. In terms of structural importance, both the top and bottom flanges are maintained, whereas the inner frame receives noticeable changes. However, at a very low volume fraction, some structural members are too small to be manufactured. Therefore, designs

at a low volume fraction may need to be modified during post-processing to address the nozzle size constraint.

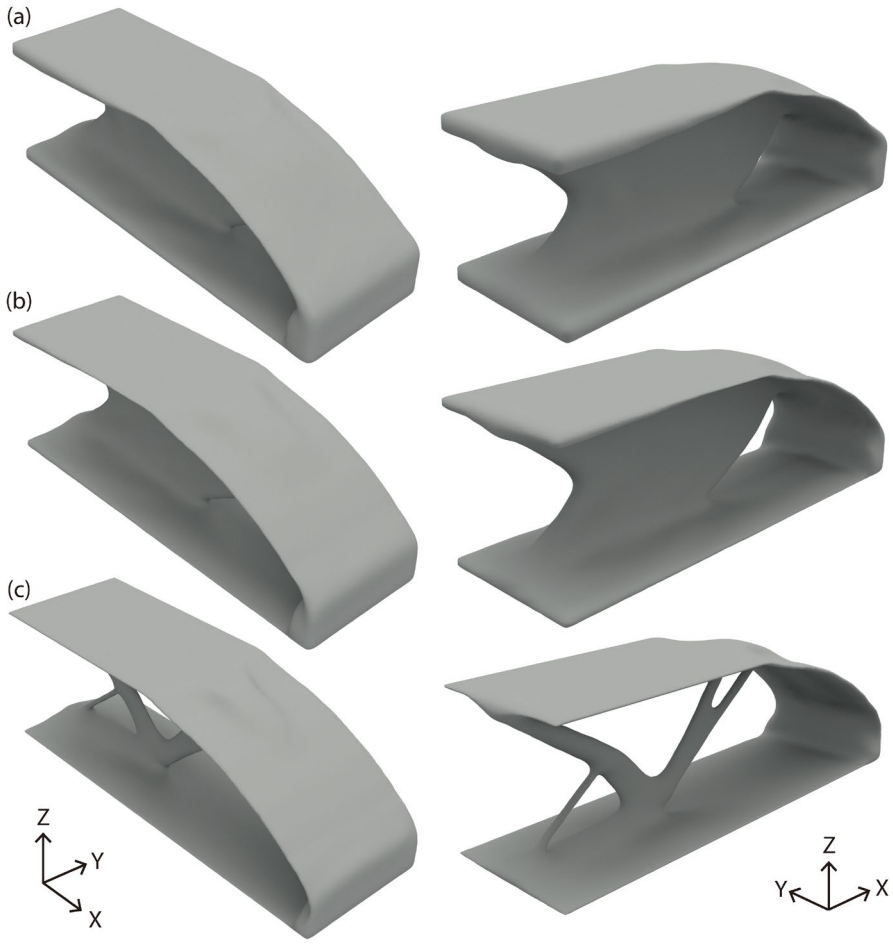

Fig. 14. Optimized designs of modular design A under low volume fractions: (a) 30%; (b) 20%; (c) 10%.

5. 3D printing process

To test the algorithm's robustness in a real design environment, it is implemented on a chair structure with a dimension of 1330 mm × 670 mm × 1000 mm. As shown in Fig. 15, the chair is fixed at the front and rear legs and uniformly loaded on the seating region. The outer part of the chair is kept unchanged as a solid non-design domain to preserve its profile, whereas the supporting region (red) is optimized based on the proposed algorithm. The design domain is discretized into cuboid mesh elements with a grid size of 10 mm, and the filter radius is specified as 30 mm. The design is split into two segments along the Y-axis, with each segment

printing from the sides towards the middle section. The Young's modulus along the horizontal plane (XZ plane) is 21.9 GPa; a lower Young's modulus is assumed for the printing direction (Y direction) as 18 GPa. The Poisson's ratio and the shear modulus are constant at 0.2 and 9.1 GPa in all directions. The evolutionary ratio is 1%, and the volume fraction is 50%. The optimized design is shown in Fig. 16, with two symmetrical components in each segment. One segment is transparent in render to show the details of the internal structure. The load on the seating region is transferred via the optimized load paths onto the front and rear legs, and the design fulfills the self-support and continuous extrusion constraints on each layer along the print direction.

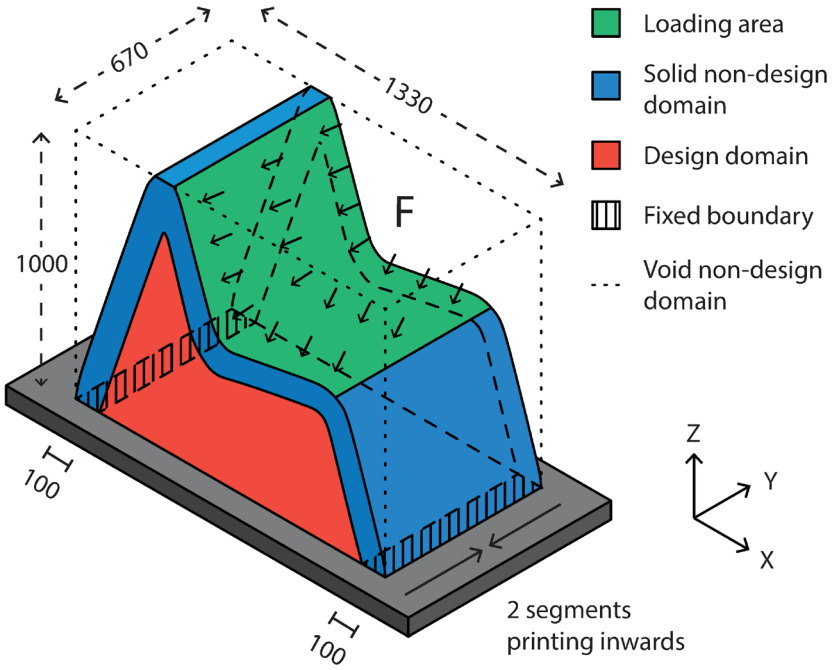

Fig. 15. Design domain of the topology optimized chair for 3DCP. A uniformly distributed load is applied perpendicular to the seating area. The chair has a fixed boundary condition at two bottom ends, and its surface is specified as the non-design domain to preserve its functionality. The optimization is carried out with two symmetrical modules on the Y-axis, with each module printing towards the centreline of the Y-axis.

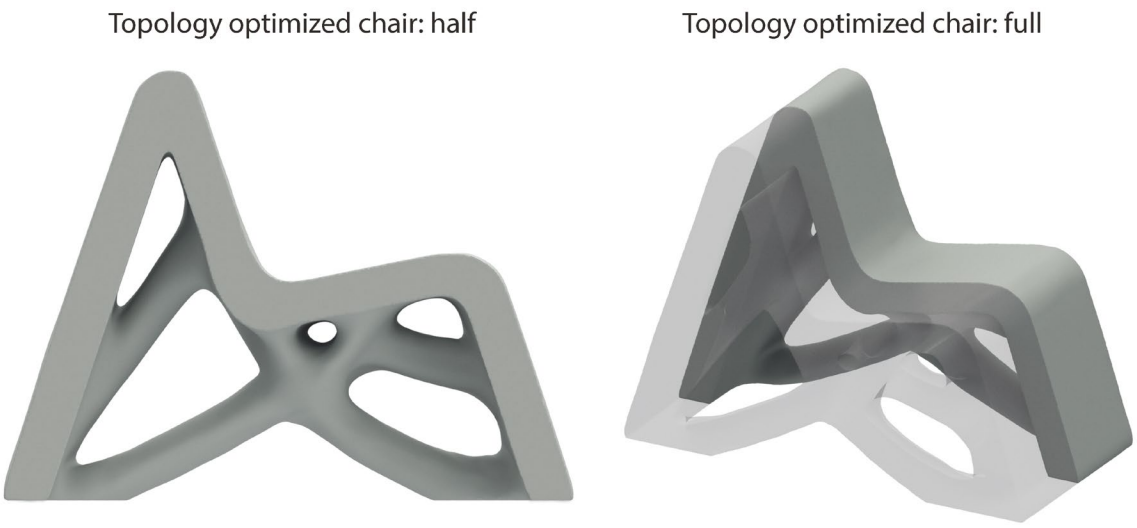

Fig. 16. A rendered view of the topology optimized chair. Two mirrored segments (solid and transparent) were printed and assembled. One mirrored segment is transparent in render to show the internal details of the structure.

Each symmetrical component is printed separately and assembled by applying high-strength chemical adhesive on its contact surface. A continuous toolpath is generated based on the author's previous work [78], and each segment is fabricated continuously without interruption. Materials used in the mixture include sand, silica fume, cement, water, polycarboxylate-based superplasticizer, and sodium gluconate retarder. The mix ratio of the raw materials can be found in Table 5. Fibers have been placed manually during the printing process to enhance the structure's tensile strength. The 4-axis robotic arm used in the experiment is Efort ER180.

Fig. 17 shows the printed outcome before and after assembly; the background is removed for better visualization. The outer surfaces of the chair have been leveled for aesthetic purposes. By successfully printing the topology optimized chair, the algorithm demonstrates its robustness in addressing various manufacturing constraints of 3DCP. By explicitly integrating the manufacturing constraints within the topology optimization framework, a continuous printing operation can be delivered with satisfactory print quality and efficiency.

Table 5: Mix design used in 3DCP.

Sand (%)	Silica fume (%)	Cement (%)	Water (%)	Superplasticizer (%)	Retarder (%)
45.4	7.8	33.3	12.7	0.6	0.2

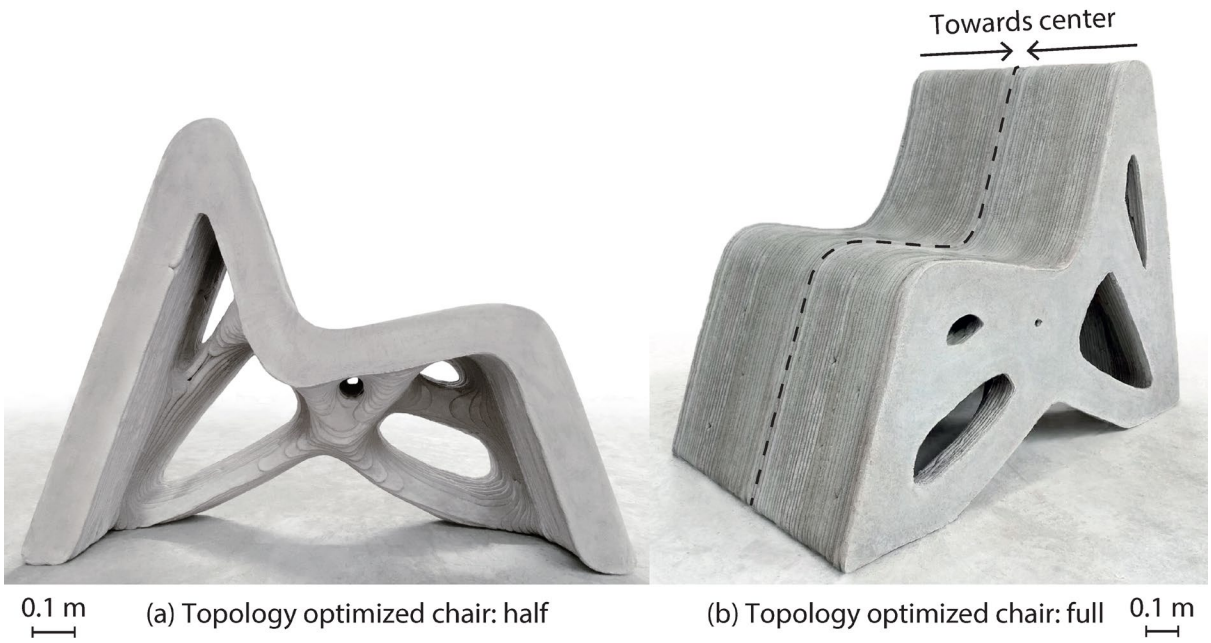

Fig. 17. 3D print result of the topology optimized chair: (a) half and (b) whole structure. Note that the scales of (a) and (b) are different.

6. Conclusion

This paper presents an innovative BESO topology optimization framework considering multiple manufacturing constraints of 3DCP. A layer-wise sensitivity scheme is proposed to satisfy the overhang angle limit of 3DCP. Vertical alignment of the optimized design along the print direction can be guaranteed, delivering a self-supporting design in the user-defined orientation. Numerical studies suggest that alternative solutions with competitive performance can be obtained using the self-support constraint. In order to facilitate continuous printing operation, a novel continuous extrusion constraint is implemented in the framework. The shortest possible routes are located based on the connected component labeling algorithm and

minimum distance principle. With interconnected 2D geometry in each layer, the optimized design achieves global geometrical continuity. Anisotropy of the 3DCP process is simulated in the optimization process by employing a transverse isotropic material model. Domain segmentation is also introduced as a design feature in the framework to mimic the modular construction concept. The design domain can be partitioned prior to the optimization process, and each segment can be assigned with its favorable print direction. The effectiveness and robustness of the proposed algorithm are further validated by generating a topology optimized chair design, which is fabricated using 3DCP in the laboratory.

The presented work focuses on the manufacturing perspective of the 3DCP processes. In future work, a stress constraint can be integrated within the topology optimization framework for a more accurate simulation. As the research in 3DCP becomes more mature, a more sophisticated self-supporting constraint capable of handling different overhang angles can be used to increase the geometrical design freedom. The approach presented in this paper can also be extended to other topology optimization methods. When more complex constraints are considered, gradient-based topology optimization methods can be more efficient.

Acknowledgment

This project was supported by the Australian Research Council (FL190100014, DP200102190) and RMIT University (Research Stipend Scholarship).

References

[1] I. Gibson, D. Rosen, B. Stucker, M. Khorasani, Additive manufacturing technologies, 3rd ed., Springer, Cham, 2021. https://doi.org/10.1007/978-3-030-56127-7.

[2] B. Blakey-Milner, P. Gradl, G. Snedden, M. Brooks, J. Pitot, E. Lopez, M. Leary, F. Berto, A. du Plessis, Metal additive manufacturing in aerospace: A review, Mater. Des. 209 (2021) 110008. https://doi.org/10.1016/j.matdes.2021.110008.

[3] J.-H. Zhu, W.-H. Zhang, L. Xia, Topology optimization in aircraft and aerospace structures design, Arch. Comput. Methods Eng. 23 (2016) 595–622.

https://doi.org/10.1007/s11831-015-9151-2.
[4] F.A.M.M. Gonçalves, A.C. Fonseca, M. Domingos, A. Gloria, A.C. Serra, J.F.J. Coelho, The potential of unsaturated polyesters in biomedicine and tissue engineering: Synthesis, structure-properties relationships and additive manufacturing, Prog. Polym. Sci. 68 (2017) 1–34. https://doi.org/10.1016/j.progpolymsci.2016.12.008.
[5] R. Leal, F.M. Barreiros, L. Alves, F. Romeiro, J.C. Vasco, M. Santos, C. Marto, Additive manufacturing tooling for the automotive industry, Int. J. Adv. Manuf. Technol. 92 (2017) 1671–1676. https://doi.org/10.1007/s00170-017-0239-8.
[6] A. Pajonk, A. Prieto, U. Blum, U. Knaack, Multi-material additive manufacturing in architecture and construction: A review, J. Build. Eng. (2021) 103603. https://doi.org/10.1016/j.jobe.2021.103603.
[7] Y. He, Y. Zhang, C. Zhang, H. Zhou, Energy-saving potential of 3D printed concrete building with integrated living wall, Energy Build. 222 (2020) 110110. https://doi.org/10.1016/j.enbuild.2020.110110.
[8] A. Anton, L. Reiter, T. Wangler, V. Frangez, R.J. Flatt, B. Dillenburger, A 3D concrete printing prefabrication platform for bespoke columns, Autom. Constr. 122 (2021) 103467. https://doi.org/10.1016/j.autcon.2020.103467.
[9] N. Gaudillière, R. Duballet, C. Bouyssou, A. Mallet, P. Roux, M. Zakeri, J. Dirrenberger, Large-scale additive manufacturing of ultra-high-performance concrete of integrated formwork for truss-shaped pillars, in: J. Willmann, P. Block, M. Hutter, K. Byrne, T. Schork (Eds.), Robot. Fabr. Archit. Art Des. 2018, Springer International Publishing, Cham, 2019: pp. 459–472. https://doi.org/10.1007/978-3-319-92294-2_35.
[10] M.P. Bendsøe, N. Kikuchi, Generating optimal topologies in structural design using a homogenization method, Comput. Methods Appl. Mech. Eng. 71 (1988) 197–224. https://doi.org/10.1016/0045-7825(88)90086-2.
[11] K. Suzuki, N. Kikuchi, A homogenization method for shape and topology optimization, Comput. Methods Appl. Mech. Eng. 93 (1991) 291–318. https://doi.org/10.1016/0045-7825(91)90245-2.
[12] M.P. Bendsøe, Optimal shape design as a material distribution problem, Struct. Optim. 1 (1989) 193–202. https://doi.org/10.1007/BF01650949.
[13] G.I.N. Rozvany, Aims, scope, methods, history and unified terminology of computer-aided topology optimization in structural mechanics, Struct. Multidiscip. Optim. 21 (2001) 90–108. https://doi.org/10.1007/s001580050174.
[14] O. Sigmund, A 99 line topology optimization code written in Matlab, Struct. Multidiscip. Optim. 21 (2001) 120–127. https://doi.org/10.1007/s001580050176.
[15] J.A. Sethian, A. Wiegmann, Structural boundary design via level set and immersed interface methods, J. Comput. Phys. 163 (2000) 489–528. https://doi.org/10.1006/jcph.2000.6581.
[16] Z. Zhuang, Y.M. Xie, S. Zhou, A reaction diffusion-based level set method using body-fitted mesh for structural topology optimization, Comput. Methods Appl. Mech. Eng. 381 (2021) 113829. https://doi.org/10.1016/j.cma.2021.113829.
[17] M.Y. Wang, X. Wang, D. Guo, A level set method for structural topology optimization, Comput. Methods Appl. Mech. Eng. 192 (2003) 227–246. https://doi.org/10.1016/S0045-7825(02)00559-5.
[18] P. Wei, M.Y. Wang, Piecewise constant level set method for structural topology optimization, Int. J. Numer. Methods Eng. 78 (2009) 379–402. https://doi.org/10.1002/nme.2478.
[19] Y.M. Xie, G.P. Steven, A simple evolutionary procedure for structural optimization, Comput. Struct. 49 (1993) 885–896. https://doi.org/10.1016/0045-7949(93)90035-C.
[20] X. Huang, Y.M. Xie, Bi-directional evolutionary topology optimization of continuum

structures with one or multiple materials, Comput. Mech. 43 (2008) 393–401. https://doi.org/10.1007/s00466-008-0312-0.
[21] O.M. Querin, G.P. Steven, Y.M. Xie, Evolutionary structural optimisation (ESO) using a bidirectional algorithm, Eng. Comput. 15 (1998) 1031–1048. https://doi.org/10.1108/02644409810244129.
[22] X. Guo, Doing topology optimization explicitly and geometrically—A new moving morphable components based framework, J. Appl. Mech. 81 (2014) 081009. https://doi.org/10.1115/1.4027609.
[23] W. Zhang, W. Yang, J. Zhou, D. Li, X. Guo, Structural topology optimization through explicit boundary evolution, J. Appl. Mech. 84 (2016). https://doi.org/10.1115/1.4034972.
[24] O. Sigmund, K. Maute, Topology optimization approaches, Struct. Multidiscip. Optim. 48 (2013) 1031–1055. https://doi.org/10.1007/s00158-013-0978-6.
[25] G.R. Zavala, A.J. Nebro, F. Luna, C.A. Coello Coello, A survey of multi-objective metaheuristics applied to structural optimization, Struct. Multidiscip. Optim. 49 (2014) 537–558. https://doi.org/10.1007/s00158-013-0996-4.
[26] Y. Xiong, S. Yao, Z.-L. Zhao, Y.M. Xie, A new approach to eliminating enclosed voids in topology optimization for additive manufacturing, Addit. Manuf. 32 (2020) 101006. https://doi.org/10.1016/j.addma.2019.101006.
[27] M. Bi, P. Tran, Y.M. Xie, Topology optimization of 3D continuum structures under geometric self-supporting constraint, Addit. Manuf. 36 (2020) 101422. https://doi.org/10.1016/j.addma.2020.101422.
[28] J. Ma, Z. Li, Z.-L. Zhao, Y.M. Xie, Creating novel furniture through topology optimization and advanced manufacturing, Rapid Prototyp. J. 27 (2021) 1749–1758. https://doi.org/10.1108/RPJ-03-2021-0047.
[29] Y. Liu, Z. Li, P. Wei, S. Chen, Generating support structures for additive manufacturing with continuum topology optimization methods, Rapid Prototyp. J. 25 (2019) 232–246. https://doi.org/10.1108/RPJ-10-2017-0213.
[30] Y.W.D. Tay, M.Y. Li, M.J. Tan, Effect of printing parameters in 3D concrete printing: Printing region and support structures, J. Mater. Process. Technol. 271 (2019) 261–270. https://doi.org/10.1016/j.jmatprotec.2019.04.007.
[31] G. Ma, Z. Li, L. Wang, F. Wang, J. Sanjayan, Mechanical anisotropy of aligned fiber reinforced composite for extrusion-based 3D printing, Constr. Build. Mater. 202 (2019) 770–783. https://doi.org/10.1016/j.conbuildmat.2019.01.008.
[32] Y. Yang, C. Wu, Z. Liu, H. Wang, Q. Ren, Mechanical anisotropy of ultra-high performance fibre-reinforced concrete for 3D printing, Cem. Concr. Compos. 125 (2022) 104310. https://doi.org/10.1016/j.cemconcomp.2021.104310.
[33] T. Marchment, J. Sanjayan, Reinforcement method for 3D concrete printing using paste-coated bar penetrations, Autom. Constr. 127 (2021) 103694. https://doi.org/10.1016/j.autcon.2021.103694.
[34] Z. Li, G. Ma, F. Wang, L. Wang, J. Sanjayan, Expansive cementitious materials to improve micro-cable reinforcement bond in 3D concrete printing, Cem. Concr. Compos. 125 (2022) 104304. https://doi.org/10.1016/j.cemconcomp.2021.104304.
[35] Y. Chen, S. He, Y. Gan, O. Çopuroğlu, F. Veer, E. Schlangen, A review of printing strategies, sustainable cementitious materials and characterization methods in the context of extrusion-based 3D concrete printing, J. Build. Eng. 45 (2022) 103599. https://doi.org/10.1016/j.jobe.2021.103599.
[36] P.F. Yuan, Q. Zhan, H. Wu, H.S. Beh, L. Zhang, Real-time toolpath planning and extrusion control (RTPEC) method for variable-width 3D concrete printing, J. Build. Eng. 46 (2022) 103716. https://doi.org/10.1016/j.jobe.2021.103716.

[37] G. Vantyghem, W. De Corte, E. Shakour, O. Amir, 3D printing of a post-tensioned concrete girder designed by topology optimization, Autom. Constr. 112 (2020) 103084. https://doi.org/10.1016/j.autcon.2020.103084.
[38] D. Asprone, F. Auricchio, C. Menna, V. Mercuri, 3D printing of reinforced concrete elements: Technology and design approach, Constr. Build. Mater. 165 (2018) 218–231. https://doi.org/10.1016/j.conbuildmat.2018.01.018.
[39] M.R. Shahmirzadi, A. Gholampour, A. Kashani, T.D. Ngo, Shrinkage behavior of cementitious 3D printing materials: Effect of temperature and relative humidity, Cem. Concr. Compos. 124 (2021) 104238. https://doi.org/10.1016/j.cemconcomp.2021.104238.
[40] T. Marchment, J. Sanjayan, Mesh reinforcing method for 3D concrete printing, Autom. Constr. 109 (2020) 102992. https://doi.org/10.1016/j.autcon.2019.102992.
[41] M.K. Mohan, A. V Rahul, G. De Schutter, K. Van Tittelboom, Extrusion-based concrete 3D printing from a material perspective: A state-of-the-art review, Cem. Concr. Compos. 115 (2021) 103855. https://doi.org/10.1016/j.cemconcomp.2020.103855.
[42] P. Shakor, J. Sanjayan, A. Nazari, S. Nejadi, Modified 3D printed powder to cement-based material and mechanical properties of cement scaffold used in 3D printing, Constr. Build. Mater. 138 (2017) 398–409. https://doi.org/10.1016/j.conbuildmat.2017.02.037.
[43] Y.W.D. Tay, G.H.A. Ting, Y. Qian, B. Panda, L. He, M.J. Tan, Time gap effect on bond strength of 3D-printed concrete, Virtual Phys. Prototyp. 14 (2019) 104–113. https://doi.org/10.1080/17452759.2018.1500420.
[44] S. Chaves Figueiredo, C. Romero Rodríguez, Z. Y. Ahmed, D.H. Bos, Y. Xu, T.M. Salet, O. Çopuroğlu, E. Schlangen, F.P. Bos, Mechanical behavior of printed strain hardening cementitious composites, Materials (Basel). 13 (2020). https://doi.org/10.3390/ma13102253.
[45] B. Panda, J.H. Lim, M.J. Tan, Mechanical properties and deformation behaviour of early age concrete in the context of digital construction, Compos. Part B Eng. 165 (2019) 563–571. https://doi.org/10.1016/j.compositesb.2019.02.040.
[46] N. Roussel, Rheological requirements for printable concretes, Cem. Concr. Res. 112 (2018) 76–85. https://doi.org/10.1016/j.cemconres.2018.04.005.
[47] R.J.M. Wolfs, F.P. Bos, T.A.M. Salet, Hardened properties of 3D printed concrete: The influence of process parameters on interlayer adhesion, Cem. Concr. Res. 119 (2019) 132–140. https://doi.org/10.1016/j.cemconres.2019.02.017.
[48] M. Sakin, Y.C. Kiroglu, 3D printing of buildings: construction of the sustainable houses of the future by BIM, Energy Procedia. 134 (2017) 702–711. https://doi.org/10.1016/j.egypro.2017.09.562.
[49] S. Lim, R.A. Buswell, T.T. Le, S.A. Austin, A.G.F. Gibb, T. Thorpe, Developments in construction-scale additive manufacturing processes, Autom. Constr. 21 (2012) 262–268. https://doi.org/10.1016/j.autcon.2011.06.010.
[50] T.A.M. Salet, Z.Y. Ahmed, F.P. Bos, H.L.M. Laagland, Design of a 3D printed concrete bridge by testing, Virtual Phys. Prototyp. 13 (2018) 222–236. https://doi.org/10.1080/17452759.2018.1476064.
[51] G. Grasser, L. Pammer, H. Köll, E. Werner, F.P. Bos, Complex architecture in printed concrete: the case of the innsbruck university 350th anniversary pavilion Cohesion, in: F.P. Bos, S.S. Lucas, R.J.M. Wolfs, T.A.M. Salet (Eds.), Second RILEM Int. Conf. Concr. Digit. Fabr., Springer International Publishing, Cham, 2020: pp. 1116–1127.
[52] J. Xiao, H. Liu, T. Ding, Finite element analysis on the anisotropic behavior of 3D printed concrete under compression and flexure, Addit. Manuf. 39 (2021) 101712. https://doi.org/10.1016/j.addma.2020.101712.
[53] J. Xiao, G. Ji, Y. Zhang, G. Ma, V. Mechtcherine, J. Pan, L. Wang, T. Ding, Z. Duan, S.

Du, Large-scale 3D printing concrete technology: Current status and future opportunities, Cem. Concr. Compos. 122 (2021) 104115. https://doi.org/10.1016/j.cemconcomp.2021.104115.
[54] A. Jipa, M. Bernhard, M. Meibodi, B. Dillenburger, 3D-printed stay-in-place formwork for topologically optimized concrete slabs, in: K. Bieg (Ed.), 2016 TxA Emerg. Des. + Technol. Conf., Texas Society of Architects, 2016: p. 107. https://doi.org/10.3929/ethz-b-000237082.
[55] A. Jipa, F. Giacomarra, R. Giesecke, G. Chousou, M. Pacher, B. Dillenburger, M. Lomaglio, M. Leschok, 3D-printed formwork for bespoke concrete stairs: from computational design to digital fabrication, in: ACM Symp. Comput. Fabr., Association for Computing Machinery, New York, NY, USA, 2019. https://doi.org/10.1145/3328939.3329003.
[56] A. Søndergaard, J. Feringa, F. Stan, D. Maier, Realization of topology optimized concrete structures using robotic abrasive wire-cutting of expanded polystyrene formwork, in: J. Willmann, P. Block, M. Hutter, K. Byrne, T. Schork (Eds.), Robot. Fabr. Archit. Art Des. 2018, Springer International Publishing, Cham, 2019: pp. 473–488.
[57] J. Burger, E. Lloret-Fritschi, F. Scotto, T. Demoulin, L. Gebhard, J. Mata-Falcón, F. Gramazio, M. Kohler, R.J. Flatt, Eggshell: ultra-thin three-dimensional printed formwork for concrete structures, 3D Print. Addit. Manuf. 7 (2020) 48–59. https://doi.org/10.1089/3dp.2019.0197.
[58] G. Vantyghem, V. Boel, W. De Corte, M. Steeman, Compliance, stress-based and multi-physics topology optimization for 3D-printed concrete structures, in: T. Wangler, R.J. Flatt (Eds.), First RILEM Int. Conf. Concr. Digit. Fabr. – Digit. Concr. 2018, Springer International Publishing, Cham, 2019: pp. 323–332.
[59] O. Amir, E. Shakour, Simultaneous shape and topology optimization of prestressed concrete beams, Struct. Multidiscip. Optim. 57 (2018) 1831–1843. https://doi.org/10.1007/s00158-017-1855-5.
[60] P. Martens, M. Mathot, F. Bos, J. Coenders, Optimising 3D printed concrete structures using topology optimisation, in: D.A. Hordijk, M. Luković (Eds.), High Tech Concr. Where Technol. Eng. Meet, Springer International Publishing, Cham, 2018: pp. 301–309.
[61] A.T. Gaynor, J.K. Guest, Topology optimization considering overhang constraints: Eliminating sacrificial support material in additive manufacturing through design, Struct. Multidiscip. Optim. 54 (2016) 1157–1172. https://doi.org/10.1007/s00158-016-1551-x.
[62] X. Qian, Undercut and overhang angle control in topology optimization: A density gradient based integral approach, Int. J. Numer. Methods Eng. 111 (2017) 247–272. https://doi.org/10.1002/nme.5461.
[63] M. Langelaar, An additive manufacturing filter for topology optimization of print-ready designs, Struct. Multidiscip. Optim. 55 (2017) 871–883. https://doi.org/10.1007/s00158-016-1522-2.
[64] M. Langelaar, Topology optimization of 3D self-supporting structures for additive manufacturing, Addit. Manuf. 12 (2016) 60–70. https://doi.org/10.1016/j.addma.2016.06.010.
[65] G. Allaire, C. Dapogny, R. Estevez, A. Faure, G. Michailidis, Structural optimization under overhang constraints imposed by additive manufacturing technologies, J. Comput. Phys. 351 (2017) 295–328. https://doi.org/10.1016/j.jcp.2017.09.041.
[66] K. Zhang, G. Cheng, L. Xu, Topology optimization considering overhang constraint in additive manufacturing, Comput. Struct. 212 (2019) 86–100. https://doi.org/10.1016/j.compstruc.2018.10.011.
[67] Y.S. Han, B. Xu, L. Zhao, Y.M. Xie, Topology optimization of continuum structures

under hybrid additive-subtractive manufacturing constraints, Struct. Multidiscip. Optim. 60 (2019) 2571–2595. https://doi.org/10.1007/s00158-019-02334-3.
[68] E. van de Ven, R. Maas, C. Ayas, M. Langelaar, F. van Keulen, Overhang control based on front propagation in 3D topology optimization for additive manufacturing, Comput. Methods Appl. Mech. Eng. 369 (2020) 113169. https://doi.org/10.1016/j.cma.2020.113169.
[69] Y. Liu, M. Zhou, C. Wei, Z. Lin, Topology optimization of self-supporting infill structures, Struct. Multidiscip. Optim. 63 (2021) 2289–2304. https://doi.org/10.1007/s00158-020-02805-y.
[70] Y. Wang, Z. Kang, Structural shape and topology optimization of cast parts using level set method, Int. J. Numer. Methods Eng. 111 (2017) 1252–1273. https://doi.org/10.1002/nme.5503.
[71] Q. Li, W. Chen, S. Liu, H. Fan, Topology optimization design of cast parts based on virtual temperature method, Comput. Aided Des. 94 (2018) 28–40. https://doi.org/10.1016/j.cad.2017.08.002.
[72] C. Wang, B. Xu, Q. Meng, J. Rong, Y. Zhao, Topology optimization of cast parts considering parting surface position, Adv. Eng. Softw. 149 (2020) 102886. https://doi.org/10.1016/j.advengsoft.2020.102886.
[73] L.N.S. Chiu, B. Rolfe, X. Wu, W. Yan, Effect of stiffness anisotropy on topology optimisation of additively manufactured structures, Eng. Struct. 171 (2018) 842–848. https://doi.org/10.1016/j.engstruct.2018.05.083.
[74] A.M. Mirzendehdel, B. Rankouhi, K. Suresh, Strength-based topology optimization for anisotropic parts, Addit. Manuf. 19 (2018) 104–113. https://doi.org/10.1016/j.addma.2017.11.007.
[75] J. Liu, A.C. To, Deposition path planning-integrated structural topology optimization for 3D additive manufacturing subject to self-support constraint, Comput. Aided Des. 91 (2017) 27–45. https://doi.org/10.1016/j.cad.2017.05.003.
[76] V.S. Papapetrou, C. Patel, A.Y. Tamijani, Stiffness-based optimization framework for the topology and fiber paths of continuous fiber composites, Compos. Part B, Eng. 183 (2020) 107681. https://doi.org/10.1016/j.compositesb.2019.107681.
[77] X. Huang, Y.M. Xie, Evolutionary topology optimization of continuum structures: methods and applications, John Wiley & Sons, Ltd, Chichester, England, 2010. https://doi.org/10.1002/9780470689486.
[78] M. Bi, L. Xia, P. Tran, Z. Li, Q. Wan, L. Wang, W. Shen, G. Ma, Y.M. Xie, Continuous contour-zigzag hybrid toolpath for large format additive manufacturing, Addit. Manuf. 55 (2022) 102822. https://doi.org/10.1016/j.addma.2022.102822.
[79] L. He, X. Ren, Q. Gao, X. Zhao, B. Yao, Y. Chao, The connected-component labeling problem: A review of state-of-the-art algorithms, Pattern Recognit. 70 (2017) 25–43. https://doi.org/10.1016/j.patcog.2017.04.018.
[80] C. Fiorio, J. Gustedt, Two linear time Union-Find strategies for image processing, Theor. Comput. Sci. 154 (1996) 165–181. https://doi.org/10.1016/0304-3975(94)00262-2.
[81] K. Wu, E. Otoo, A. Shoshani, Optimizing connected component labeling algorithms, in: SPIE, 2005: pp. 1965–1976. https://doi.org/10.1117/12.596105.
[82] M. van den Heever, F. Bester, J. Kruger, G. van Zijl, Mechanical characterisation for numerical simulation of extrusion-based 3D concrete printing, J. Build. Eng. 44 (2021) 102944. https://doi.org/10.1016/j.jobe.2021.102944.